

# Accepted Manuscript

The extended distributed microstructure model for gradient-driven transport: A two-scale model for bypassing effective parameters

E.J. Carr, P. Perré, I.W. Turner

PII: S0021-9991(16)30497-1  
DOI: <http://dx.doi.org/10.1016/j.jcp.2016.10.004>  
Reference: YJCPH 6881

To appear in: *Journal of Computational Physics*

Received date: 10 December 2015  
Revised date: 31 May 2016  
Accepted date: 2 October 2016

Please cite this article in press as: E.J. Carr et al., The extended distributed microstructure model for gradient-driven transport: A two-scale model for bypassing effective parameters, *J. Comput. Phys.* (2016), <http://dx.doi.org/10.1016/j.jcp.2016.10.004>

This is a PDF file of an unedited manuscript that has been accepted for publication. As a service to our customers we are providing this early version of the manuscript. The manuscript will undergo copyediting, typesetting, and review of the resulting proof before it is published in its final form. Please note that during the production process errors may be discovered which could affect the content, and all legal disclaimers that apply to the journal pertain.



# The extended distributed microstructure model for gradient-driven transport: A two-scale model for bypassing effective parameters

E. J. Carr<sup>a,b,\*</sup>, P. Perré<sup>b</sup>, I. W. Turner<sup>a,c</sup>

<sup>a</sup>*School of Mathematical Sciences, Queensland University of Technology (QUT), Brisbane, Australia*

<sup>b</sup>*LGPM, CentraleSupélec, Université Paris-Saclay, Chatenay-Malabry, France*

<sup>c</sup>*Australian Research Council Centre of Excellence for Mathematical and Statistical Frontiers (ACEMS), Queensland University of Technology (QUT), Brisbane, Australia*

---

## Abstract

Numerous problems involving gradient-driven transport processes—e.g., Fourier’s and Darcy’s law—in heterogeneous materials concern a physical domain that is much larger than the scale at which the coefficients vary spatially. To overcome the prohibitive computational cost associated with such problems, the well-established Distributed Microstructure Model (DMM) provides a two-scale description of the transport process that produces a computationally cheap approximation to the fine-scale solution. This is achieved via the introduction of sparsely distributed micro-cells that together resolve small patches of the fine-scale structure: a macroscopic equation with an effective coefficient describes the global transport and a microscopic equation governs the local transport within each micro-cell. In this paper, we propose a new formulation, the Extended Distributed Microstructure Model (EDMM), where the macroscopic flux is instead defined as the average of the microscopic fluxes within the micro-cells. This avoids the need for any effective parameters and more accurately accounts for a non-equilibrium field in the micro-cells. Another important contribution of the work is the presentation of a new and improved numerical scheme for performing the two-scale computations using control volume, Krylov subspace and parallel computing techniques. Numerical tests are carried out on two challenging test problems: heat conduction in a composite medium and unsaturated water flow in heterogeneous soils. The results indicate that while DMM is more efficient, EDMM is more accurate and is able to capture additional fine-scale features in the solution.

**Keywords:** two-scale, multiscale, microstructure, dual-scale, heterogeneous, homogenization

---

## 1. Introduction

Many transport/flow problems in heterogeneous materials involve a physical domain that is much larger than the scale at which material properties (e.g. conductivity) vary spatially. A good example of this is a heterogeneous aquifer containing small clay lenses embedded in sand, which are much

---

\*Corresponding author

Email addresses: [elliott.carr@qut.edu.au](mailto:elliott.carr@qut.edu.au) (E. J. Carr), [patrick.perre@centrelasupelec.fr](mailto:patrick.perre@centrelasupelec.fr) (P. Perré), [i.turner@qut.edu.au](mailto:i.turner@qut.edu.au) (I. W. Turner)

Preprint submitted to J. Comput. Phys.

October 3, 2016

smaller than the size of the aquifer. In such problems, numerical solution of the governing PDE is infeasible due to the massive amount of computational resources required to mesh the heterogeneous geometry and step the solution in time.

A common workaround to solving the fine-scale model is to adopt a larger, macroscopic scale of description by treating the heterogeneous material as a homogeneous material [3, 32]. The governing macroscopic equation typically resembles the form of the fine-scale equation with the exception that the material properties varying on the fine-scale (microscopic scale) are replaced with smoothed effective properties. A problem with this approach, however, is that it provides no information on the field at the microscopic scale of the heterogeneities and can be inadequate for problems where the material properties differ by several orders of magnitude [26]. Such limitations have led to the development of two-scale models that describe the transport processes on two scales—macroscopic and microscopic.

The underlying motivation behind a two-scale model is that solving the fine-scale equation on the heterogeneous geometry within a number of small domains (micro-cells) sparsely distributed throughout the full domain, coupled in a suitable manner, is much less expensive than solving the fine-scale equation on the full heterogeneous geometry. This is particularly true in the case of coupled heat and mass transfer [19]. Compared to a classical macroscopic approach, the concept of multiscale modeling allows a two-way coupling throughout the configuration of interest: (i) microscopic phenomena whose time constants are relevant at the macroscopic scale can be considered and (ii) information of the field at the level of heterogeneities can be obtained. The first step is usually to generate a coarse macroscopic mesh over the domain that is considerably more coarse than the very fine mesh required to capture the fine structure of the heterogeneous geometry. The challenges are then to (i) derive or propose the form of the macroscopic equation (if necessary) (ii) decide where to position the micro-cells in relation to the macroscopic mesh (iii) determine how the two scales are coupled, and (iv) determine the form of the boundary conditions for the micro-cell problems in such a way that the solution on each micro-cell mimics the solution of the full problem as if it were embedded in the full domain.

This paper is devoted to two-scale modeling of the following transport equation:

$$\frac{\partial \psi}{\partial t} + \nabla \cdot \mathbf{q} = 0, \quad \text{in } \Omega, \quad (1)$$

where the domain  $\Omega \subset \mathbb{R}^d$  ( $d = 2, 3$ ) is composed of  $p$  sub-domains  $\Omega_i$  ( $i = 1, \dots, p$ ) each occupied by homogeneous material,  $\psi$  is the conserved quantity,  $\mathbf{q}$  is the flux vector and  $t$  is time. The problem is closed by introducing constitutive laws which relate  $\psi$  and  $\mathbf{q}$  with a scalar field  $u(x, t)$ . Within sub-domain  $\Omega_i$ , the quantity  $\psi$  is given in terms of a known function  $f_i$  of  $u$ , that is  $\psi = f_i(u)$  while the flux is assumed to be of the form of standard nonlinear diffusion  $\mathbf{q} = K_i(u) \nabla u$  in  $\Omega_i$  (e.g., Fick's, Fourier's or Darcy's law for the flux). In this case,  $u$  represents, for example, density, temperature or pressure and  $K_i$  is the diffusivity/conductivity (we will refer to this as the conductivity hereafter), a known function of  $u$  that depends on the properties of the material occupying  $\Omega_i$ . Clearly, if the size of some of the sub-domains  $\Omega_i$  are very small relative to the size of the domain  $\Omega$ , numerical solution of equation (1) is prohibitively expensive. Some examples of two-scale approaches for such problems include the:

1. Heterogeneous multiscale method (HMM) (and similar methods) [1, 7–11, 33, 34] where a macroscopic field is evolved on the coarse mesh with unknown macroscopic flux recovered from the

solution of the fine-scale equations on micro-cells that have been strategically positioned at locations where macroscopic flux information is required (e.g., at the midpoint between two neighboring nodes when using a finite difference discretization in space).

2. Distributed microstructure model (DMM) (also called double porosity or dual porosity model) [4, 17, 23, 26, 27], which is applicable to the specific case where the domain  $\Omega$  is composed of two sub-domains occupied by homogeneous material ( $p = 2$ ), where one is connected and the other forms isolated/disconnected inclusions (see Figure 1). A macroscopic equation with an effective conductivity describes the global transport in the connected sub-domain and a microscopic equation (taking the form of equation 1) governs the local transport in the inclusions.
3. “Equation-free” approach (including related methods such as the gap-tooth scheme and patch dynamics) [9, 14, 15, 20–22], which evolves the macroscopic field on the coarse mesh using only appropriately initialized micro-cell problems, bypassing the use of a macroscopic equation.

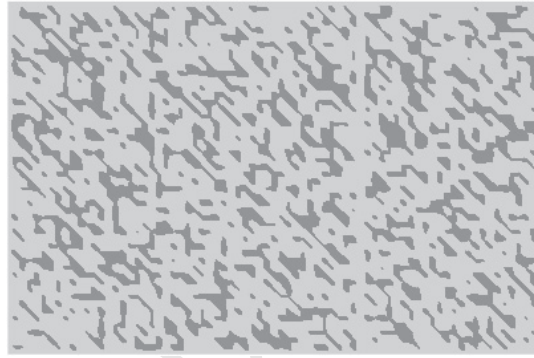


Figure 1: Binary medium composed of two sub-domains occupied by homogeneous material, where one material is connected (light gray sub-domain) and the other forms isolated/disconnected inclusions (dark gray sub-domain).

In this paper, we focus on the second approach, where coupling between scales occurs on the interface between the two sub-domains within each micro-cell: a Dirichlet condition is specified equating the microscopic and macroscopic variables and the average microscopic flux across the interface is included as a source term in the macroscopic equation (representing transfer between the two materials). Such models first appeared in the literature in the early 90s [2, 23, 24], however, these early papers mainly addressed theoretical aspects due to the prohibitive cost of implementing the models in a computational code. Numerical results have since been published for modelling unsaturated water flow in heterogeneous soils using Richards’ equation. Szymkiewicz, Lewandowska and co-authors presented numerical simulations for simple inclusion geometries, including circular [26], rectangular [27], spherical [28] and staggered rectangular [27]. A one-dimensional numerical scheme was used at the microscale, which led to an overestimation of water flow into the inclusions by as much as 5% over the a 25 hour simulation. More recently, Carr and Turner [4] developed a new numerical scheme for carrying out the two-scale computations using unstructured meshes at both scales, which permitted application of the model to irregular inclusions geometries.

A limitation of DMM is that it requires two separate calculations on the micro-cell: one to compute the effective conductivity assuming local equilibrium and another to compute the microscopic field in the inclusions within each micro-cell. Due to the assumption of equilibrium in the connected

sub-domain within the micro-cell, the approach is also only applicable to the binary medium configuration outlined above, where the material occupying the connected sub-domain is highly conductive compared to the material occupying the inclusions. The ultimate goal of two-scale modeling is to develop an approach suitable for a completely general domain  $\Omega$ —for example, both sub-domains connected, more than two materials, any contrast of material properties, etc. For such an approach we believe that one must solve the fine-scale (microscale) equation (1) on the full micro-cell. As an intermediate step towards this long term goal, we propose the *Extended* DMM (EDMM), which extends the computation performed at the microscale to the full micro-cell. This allows the macroscopic flux to be defined as the average of the microscopic fluxes and computed using the local field in the micro-cell, avoiding the need for the effective (macroscopic) conductivity. The new approach can also be thought of as a hybrid of HMM and DMM.

A second important contribution of this work is the presentation of a new and improved numerical scheme for performing the two-scale computations, which offers two key developments on the method proposed by Carr and Turner [4]. The first development is to center the micro-cells around the centroids of each macroscopic element (demonstrated in Figures 3 and 4 for DMM and EDMM, respectively) rather than around the macroscopic nodes. This overcomes the issue that occurs at the macroscopic boundary nodes where part of the micro-cell incorrectly lies outside the domain  $\Omega$ . The second development is to supply the value for the microscale Dirichlet boundary condition by constructing an interpolating function of the macroscopic field. The new approach more accurately captures the direction of the flow in the micro-cell, ensures the microscopic field is suitably bounded by the macroscopic field and permits the two-scale model to be correctly validated against the fine-scale model for a periodic medium (see Section 4).

The remaining sections of this paper are organised as follows. In Sections 2.1 and 2.2, we summarize the fine-scale model in a binary medium based on the transport equation (1) and discuss macroscopic averaging of the fine-scale equations before going on to present a classical macroscopic model (Section 2.3), distributed microstructure model (Section 2.4) and the new extended distributed microstructure model (Section 3). Section 4 describes the numerical scheme for carrying out two-scale computations in full detail including mesh configuration, spatial discretization, coupling between scales, time stepping and code implementation. In Section 5, the two-scale computational code is applied to two challenging test cases: heat conduction in a composite material and unsaturated water flow in a two-soil system. The accuracy and computational efficiency of the two-scale numerical solutions are assessed against solutions to the fine-scale model and the macroscopic model. Future research directions and a summary of the work is given in Section 6.

## 2. Classical Models

### 2.1. Fine-scale Model

Consider a binary medium  $\Omega \subset \mathbb{R}^d$  ( $d = 2, 3$ ) composed of two materials. The parts of  $\Omega$  occupied by material  $a$  and material  $b$  are denoted by  $\Omega_a$  and  $\Omega_b$ , respectively, while  $\Gamma$  is the interface between the two sub-domains. Throughout this work, we make the simplifying assumption that  $\Omega_a$  is connected while  $\Omega_b$  forms isolated/disconnected inclusions that are interior to  $\Omega$ . Let  $\psi_i$ ,  $\mathbf{q}_i$  and  $u_i$  denote, respectively, the conserved quantity, flux and scalar unknown in  $\Omega_i$  ( $i = a, b$ ). The

governing equations are summarized as follows:

$$\frac{\partial \psi_a}{\partial t} + \nabla \cdot \mathbf{q}_a = 0 \quad \text{in } \Omega_a \quad (2a)$$

$$\frac{\partial \psi_b}{\partial t} + \nabla \cdot \mathbf{q}_b = 0 \quad \text{in } \Omega_b \quad (2b)$$

$$u_a = u_b \quad \text{on } \Gamma \quad (2c)$$

$$\mathbf{q}_a \cdot \mathbf{n} = \mathbf{q}_b \cdot \mathbf{n} \quad \text{on } \Gamma \quad (2d)$$

where  $\mathbf{n}$  is the unit vector normal to  $\Gamma$  directed outward from  $\Omega_b$ . In addition to applying external boundary conditions on the boundary of  $\Omega$ —denoted hereafter by  $\partial\Omega$ —the governing equations are coupled with appropriate internal boundary conditions on the interface  $\Gamma$  between the two sub-domains: both the scalar unknown and flux are assumed continuous (2c)–(2d). The following constitutive laws are used to close the model:

$$\psi_a = f_a(u_a), \quad \psi_b = f_b(u_b), \quad \mathbf{q}_a = -K_a(u_a)\nabla u_a, \quad \mathbf{q}_b = -K_b(u_b)\nabla u_b, \quad (2e)$$

where  $f_a$ ,  $f_b$ ,  $K_a$  and  $K_b$  are known functions. We will refer to  $K_a$  and  $K_b$  as conductivities and assume that  $K_b \leq K_a$ .

## 2.2. Macroscopic averaging

When the scale of the heterogeneities is very small (i.e., when the size of the inclusions  $\Omega_b$  are very small relative to the size of the domain  $\Omega$ ), numerical solution of the fine-scale model (2) is prohibitively expensive due to the massive amount of computational resources required to mesh the intricate heterogeneous geometry and evolve the solution in time. In this case, an averaging approach transforms the governing set of equations (2) from equations defined in terms of microscopic variables only to equations defined in terms of macroscopic and microscopic variables. This is accomplished by associating a representative elementary volume or *micro-cell*  $\mathcal{C}_x \subset \Omega$  with every point in space ( $x \in \Omega$ ). At each  $x \in \Omega$ , the micro-cell, which doesn't necessarily have the same geometry at each  $x$ , provides the fine-scale structure in a small region around  $x$ . The parts of  $\mathcal{C}_x$  occupied by material  $a$  and material  $b$  are denoted by  $\mathcal{C}_{x,a} = \Omega_a \cap \mathcal{C}_x$  and  $\mathcal{C}_{x,b} = \Omega_b \cap \mathcal{C}_x$ , respectively, while  $\Gamma_x$  is the interface between the two sub-domains within  $\mathcal{C}_x$ . We assume that  $\mathcal{C}_{x,b}$  is entirely located in the interior of the micro-cell  $\mathcal{C}_x$ <sup>1</sup>.

The equations (2a) are averaged over the micro-cell as follows:

$$\frac{1}{|\mathcal{C}_x|} \int_{\mathcal{C}_{x,i}} \frac{\partial \psi_i}{\partial t} dV + \frac{1}{|\mathcal{C}_x|} \int_{\mathcal{C}_{x,i}} (\nabla \cdot \mathbf{q}_i) dV = 0, \quad i = a, b, \quad (3)$$

where  $|\mathcal{C}_x|$  is the volume of  $\mathcal{C}_x$ . The temporal averaging theorem relates the average of the temporal derivative of the microscopic variable to the temporal derivative of the macroscopic (averaged) variable:

$$\int_{\mathcal{C}_{x,i}} \frac{\partial \psi_i}{\partial t} dV = \frac{\partial}{\partial t} \left( \int_{\mathcal{C}_{x,i}} \psi_i dV \right), \quad i = a, b. \quad (4)$$

<sup>1</sup>We note that smaller or large micro-cells associated with the same point  $x \in \Omega$  may not satisfy this constraint.

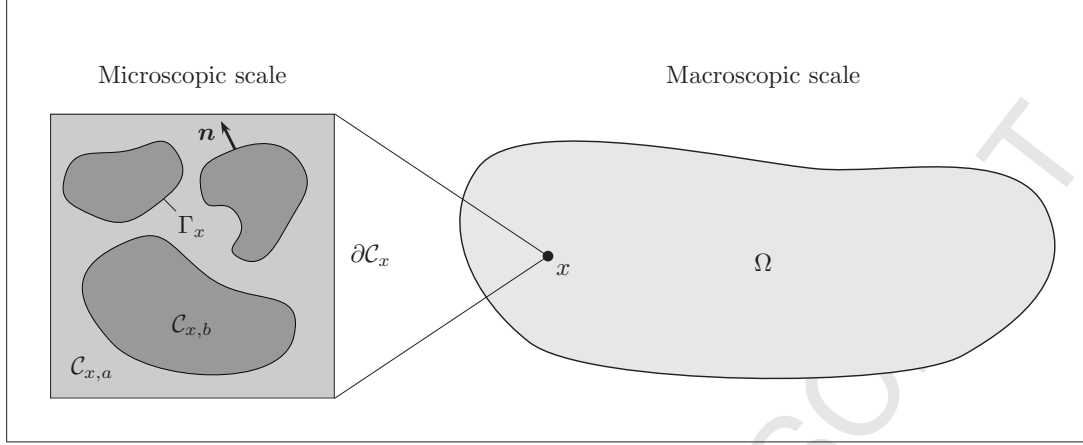


Figure 2: Two-scale configuration: at each point  $x \in \Omega$ , there exists a micro-cell  $\mathcal{C}_x$ .

For material  $a$ , the spatial averaging theorem allows the average of the divergence of the microscopic flux to be expressed in terms of the divergence of the macroscopic (averaged) flux [31]:

$$\frac{1}{|\mathcal{C}_x|} \int_{\mathcal{C}_{x,a}} (\nabla \cdot \mathbf{q}_a) dV = \nabla_x \cdot \left( \frac{1}{|\mathcal{C}_x|} \int_{\mathcal{C}_{x,a}} \mathbf{q}_a dV \right) - \frac{1}{|\mathcal{C}_x|} \int_{\Gamma_x} \mathbf{q}_a \cdot \mathbf{n} ds$$

where  $\mathbf{n}$  is the unit vector normal to  $\Gamma_x$  direct outward from  $\mathcal{C}_{x,b}$  and the subscript on the gradient indicates that the operator is taken with respect to the macroscopic spatial variable  $x$ . For material  $b$ , since  $\mathcal{C}_{x,b}$  does not intersect the external boundary of the micro-cell ( $\partial\mathcal{C}_x$ ), we can simply use the divergence theorem:

$$\frac{1}{|\mathcal{C}_x|} \int_{\mathcal{C}_{x,b}} (\nabla \cdot \mathbf{q}_b) dV = \frac{1}{|\mathcal{C}_x|} \int_{\Gamma_x} \mathbf{q}_b \cdot \mathbf{n} ds.$$

In summary, the follow pair of macroscopic (averaged) equations are obtained

$$\frac{|\mathcal{C}_{x,a}|}{|\mathcal{C}_x|} \frac{\partial}{\partial t} \left( \frac{1}{|\mathcal{C}_{x,a}|} \int_{\mathcal{C}_{x,a}} \psi_a dV \right) + \nabla_x \cdot \left( \frac{1}{|\mathcal{C}_x|} \int_{\mathcal{C}_{x,a}} \mathbf{q}_a dV \right) - \frac{1}{|\mathcal{C}_x|} \int_{\Gamma_x} \mathbf{q}_a \cdot \mathbf{n} ds = 0 \quad (5a)$$

$$\frac{|\mathcal{C}_{x,b}|}{|\mathcal{C}_x|} \frac{\partial}{\partial t} \left( \frac{1}{|\mathcal{C}_{x,a}|} \int_{\mathcal{C}_{x,a}} \psi_a dV \right) + \frac{1}{|\mathcal{C}_x|} \int_{\Gamma_x} \mathbf{q}_b \cdot \mathbf{n} ds = 0 \quad (5b)$$

where  $|\mathcal{C}_{x,i}|$  is the volume of  $\mathcal{C}_{x,i}$  for  $i = a, b$ . Introducing the macroscopic (averaged) variables:

$$\Psi_a = \frac{1}{|\mathcal{C}_{x,a}|} \int_{\mathcal{C}_{x,a}} \psi_a dV, \quad \Psi_b = \frac{1}{|\mathcal{C}_{x,b}|} \int_{\mathcal{C}_{x,b}} \psi_b dV, \quad (6)$$

$$\mathbf{Q}_a = \frac{1}{|\mathcal{C}_x|} \int_{\mathcal{C}_{x,a}} \mathbf{q}_a dV, \quad S = \frac{1}{|\mathcal{C}_x|} \int_{\Gamma_x} \mathbf{q}_a \cdot \mathbf{n} ds = \frac{1}{|\mathcal{C}_x|} \int_{\Gamma_x} \mathbf{q}_b \cdot \mathbf{n} ds \quad (7)$$

allows the equations (5) to be expressed succinctly as follows:

$$\varepsilon_a \frac{\partial \Psi_a}{\partial t} + \nabla_x \cdot \mathbf{Q}_a = S \quad (8a)$$

$$\varepsilon_b \frac{\partial \Psi_b}{\partial t} = -S \quad (8b)$$



where the volume fractions are defined by  $\varepsilon_i = |\mathcal{C}_{x,i}|/|\mathcal{C}_x|$  for  $i = a, b$  and the source term  $S$  quantifies the exchange of fluid/mass between the two materials. Note that the definition of the source term (7) follows from continuity of the flux at the interface as described in equation (2d). Alternatively, applying the divergence theorem and the temporal averaging theorem, we have:

$$S = \frac{1}{|\mathcal{C}_x|} \int_{\mathcal{C}_{x,b}} \nabla \cdot \mathbf{q}_b dV = -\frac{1}{|\mathcal{C}_x|} \int_{\mathcal{C}_{x,b}} \frac{\partial \psi_b}{\partial t} dV = -\frac{1}{|\mathcal{C}_x|} \frac{\partial}{\partial t} \int_{\mathcal{C}_{x,b}} \psi_b dV = -\varepsilon_b \frac{\partial \Psi_b}{\partial t}, \quad (9)$$

which is easily seen from (8b).

### 2.3. Macroscale Model

We define the following macroscopic model for (2):

$$\frac{\partial}{\partial t} [\varepsilon_a \Psi_a + \varepsilon_b \Psi_b] + \nabla_x \cdot \mathbf{Q}_a = 0, \quad x \in \Omega, \quad (10)$$

where  $\Psi_a = f_a(U_a)$  and  $\Psi_b = f_b(U_a)$  and  $U_a$  is the macroscopic scalar unknown, while the macroscopic flux assumed to take the form:

$$\mathbf{Q}_a = -\mathbf{K}_{\text{eff}}(U_a) \nabla_x U_a, \quad (11)$$

where  $\mathbf{K}_{\text{eff}}$  is the effective conductivity. The initial and boundary conditions are assumed to be the same as those for the fine-scale model (2). The macroscopic model is usually only suitable when  $K_a$  and  $K_b$  are roughly of the same order of magnitude. Under these circumstances, the problem is almost homogeneous  $u_b \simeq u_a$  and hence nearly purely macroscopic (i.e. the field in  $\mathcal{C}_{x,b}$  equilibrates at a fast rate meaning that  $u_b$  quickly attains the value of  $u_a$  imposed at the interface  $\Gamma_x$ ). In this case, the assumption  $u_b = U_a$  in  $\mathcal{C}_{x,b}$  is reasonable and the source term (9) in (8a) becomes:

$$S = -\frac{1}{|\mathcal{C}_x|} \frac{\partial}{\partial t} \int_{\mathcal{C}_{x,b}} \psi_b dV = -\frac{|\mathcal{C}_{x,b}|}{|\mathcal{C}_x|} \frac{\partial}{\partial t} f_b(U_a) = -\varepsilon_b \frac{\partial \Psi_b}{\partial t},$$

which explains the additional contribution to the accumulation term in equation (10). Alternatively, one may think of (10) as the sum of the macroscopic averaged equations for material  $a$  and  $b$  (8). However, the definition of the macroscopic flux  $\mathbf{Q}_a$  must include the contribution of the flux over  $\mathcal{C}_{x,b}$  in addition to  $\mathcal{C}_{x,a}$ . To see why, suppose  $\mathbf{q}_a$  and  $\mathbf{q}_b$  are both equal to the same constant vector within the micro-cell. In this case,  $\mathbf{Q}_a$  defined according to equation (7) is not equal to that constant vector.

According to the homogenization theory [16, 25, 26], at each point  $x \in \Omega$ , the  $j$ th column of the effective conductivity  $\mathbf{K}_{\text{eff}} \in \mathbb{R}^{d \times d}$  can be computed for a given value of  $U_a$  using the following formula:

$$[\mathbf{K}_{\text{eff}}(U_a)]_{*j} = \frac{1}{|\mathcal{C}_x|} \left( \int_{\mathcal{C}_{x,a}} \hat{K}_a \nabla_y (\chi_a + y_j) dV + \int_{\mathcal{C}_{x,b}} \hat{K}_b \nabla_y (\chi_b + y_j) dV \right), \quad (12)$$



for  $j = 1, \dots, d$ , where  $\hat{K}_a = K_a(U_a)$  and  $\hat{K}_b = K_b(U_a)$ , and  $\chi_a$  and  $\chi_b$  are the solutions of the following *micro-cell problem*:

$$\nabla_y \cdot (\hat{K}_a \nabla_y (\chi_a + y_j)) = 0, \quad y \in \mathcal{C}_{x,a} \quad (13a)$$

$$\nabla_y \cdot (\hat{K}_b \nabla_y (\chi_b + y_j)) = 0, \quad y \in \mathcal{C}_{x,b} \quad (13b)$$

$$\chi_a = \chi_b, \quad y \in \Gamma_x \quad (13c)$$

$$\hat{K}_a \nabla_y (\chi_a + y_j) \cdot \mathbf{n} = \hat{K}_b \nabla_y (\chi_b + y_j) \cdot \mathbf{n}, \quad y \in \Gamma_x \quad (13d)$$

$$\frac{1}{|\mathcal{C}_x|} \int_{\mathcal{C}_{x,a}} \chi_a dV + \frac{1}{|\mathcal{C}_x|} \int_{\mathcal{C}_{x,b}} \chi_b dV = 0 \quad (13e)$$

with periodic boundary conditions. For general non-constant functions  $K_a(\cdot)$  and  $K_b(\cdot)$  the effective parameter depends on the value of the macroscopic unknown  $U_a$ . Rather than solve this problem and compute  $\mathbf{K}_{\text{eff}}$  via (12) for each new value of  $U_a$  throughout the simulation, standard practice is to compute  $\mathbf{K}_{\text{eff}}$  for a suitable sequence of  $N$  discrete values of  $U_a$  and then use interpolation to evaluate  $\mathbf{K}_{\text{eff}}$  at any  $U_a$  [4, 27]. In this case, for each cell  $\mathcal{C}_x$ , a solution of the micro-cell problem (13) must be found for each combination of  $j = 1, \dots, d$  and discrete value of  $U_a$ , which represents a pre-processing cost of  $N \times d \times m$  cell problems, where  $m$  is the number of micro-cells.

#### 2.4. The Distributed Microstructure Model - A Two-Scale Model for Binary Media

The distributed microstructure model (DMM) for describing the fine-scale system (2) can be summarized by the following coupled system of macroscopic and microscopic equations [4, 17, 23, 26]:

$$\varepsilon_a \frac{\partial \Psi_a}{\partial t} + \nabla_x \cdot \mathbf{Q}_a = S, \quad x \in \Omega \quad (14a)$$

$$\frac{\partial \psi_b}{\partial t} + \nabla_y \cdot \mathbf{q}_b = 0, \quad y \in \mathcal{C}_{x,b} \quad (14b)$$

$$u_b = U_a, \quad y \in \Gamma_x \quad (14c)$$

$$S = \frac{1}{|\mathcal{C}_x|} \int_{\Gamma_x} \mathbf{q}_b \cdot \mathbf{n} ds \quad (14d)$$

where  $\Psi_a = f_a(U_a)$  and  $U_a$  is the macroscopic scalar unknown in material  $a$ , while the macroscopic flux is defined as

$$\mathbf{Q}_a = -\mathbf{K}_{\text{eff}}(U_a) \nabla_x U_a, \quad (15)$$

where  $\mathbf{K}_{\text{eff}}$  is the effective conductivity as defined in equation (12). The macroscopic equation (14a) describes the global transport in material  $a$  only and resembles the macroscopic (averaged) equation (8a). The initial and boundary conditions for the macroscopic equation (14a) are the same as those for the fine-scale model (2). At the microscale, DMM assumes equilibrium in material  $a$  only, that is,  $u_a = U_a$  in  $\mathcal{C}_{x,a}$ . The source term  $S$  is defined as it is in equation (7), that is, as the flux passing through the interface  $\Gamma_x$  scaled by the micro-cell volume  $|\mathcal{C}_x|$ . Thus, at each point  $x \in \Omega$  and time  $t$ , in order to compute  $S$  one has to solve the local transport equation on  $\mathcal{C}_{x,b}$  (14b). Following the interface condition applied in the fine-scale model (2c), additional coupling between the scales is imposed along the interface  $\Gamma_x$  via a Dirichlet boundary condition matching the microscopic and macroscopic variables (14c).

### 3. The Extended Distributed Microstructure Model - Bypassing Effective Parameters

DMM, as outlined in the previous section, suffers from three major drawbacks:

- (i) It is suitable only for the specific case of a binary medium as discussed in Sections 2.1 and 2.2, where  $\Omega_a$  is connected,  $\Omega_b$  forms isolated/disconnected inclusions that are interior to  $\Omega$ , and  $\mathcal{C}_{x,b}$  does not intersect the external surface  $\partial\mathcal{C}_x$  of the micro-cell  $\mathcal{C}_x$ . Nowhere does the model permit for macroscopic transport to take place in  $\Omega_b$ .
- (ii) It requires two separate calculations on the micro-cell: one to compute the effective conductivity  $\mathbf{K}_{\text{eff}}$  and another to compute the microscopic field within  $\mathcal{C}_{x,b}$ .
- (iii) Since it assumes equilibrium in  $\mathcal{C}_{x,a}$  at the microscale, it is suitable for the specific case where material  $a$  is highly conductive compared to material  $b$ , which means that it is less applicable as the conductivity in material  $b$  ( $K_b$ ) approaches the value of the conductivity in material  $a$  ( $K_a$ ).

The ultimate goal of two-scale modeling is to develop an approach suitable for a completely general configuration (both materials connected<sup>2</sup>, more than two materials, etc.). For such an approach one must extend the computation performed at the microscale to the full cell  $\mathcal{C}_x$ . As an intermediate step towards this long term goal, we propose the *Extended* Distributed Microstructure Model (EDMM), which can be summarized by the following coupled system of macroscopic and microscopic equations:

$$\varepsilon_a \frac{\partial \Psi_a}{\partial t} + \nabla_x \cdot \mathbf{Q}_a = S, \quad x \in \Omega \quad (16a)$$

$$\frac{\partial \psi_a}{\partial t} + \nabla_y \cdot \mathbf{q}_a = 0, \quad y \in \mathcal{C}_{x,a} \quad (16b)$$

$$\frac{\partial \psi_b}{\partial t} + \nabla_y \cdot \mathbf{q}_b = 0, \quad y \in \mathcal{C}_{x,b} \quad (16c)$$

$$u_a = u_b, \quad y \in \Gamma_x \quad (16d)$$

$$\mathbf{q}_a \cdot \mathbf{n} = \mathbf{q}_b \cdot \mathbf{n}, \quad y \in \Gamma_x \quad (16e)$$

$$u_a = U_a, \quad y \in \partial\mathcal{C}_x \quad (16f)$$

$$S = \frac{1}{|\mathcal{C}_x|} \int_{\Gamma_x} \mathbf{q}_b \cdot \mathbf{n} \, ds \quad (16g)$$

$$\mathbf{Q}_a = \frac{1}{|\mathcal{C}_x|} \left( \int_{\mathcal{C}_{x,a}} \mathbf{q}_a \, dV + \int_{\mathcal{C}_{x,b}} \mathbf{q}_b \, dV \right) \quad (16h)$$

Here, the global transport in the connected material  $a$  is described at the macro-scale by an equation similar in appearance to (14a). Indeed, the accumulation term and source term remain unchanged. However, in contrast to DMM, EDMM computes the microscopic field over the entire cell  $\mathcal{C}_x$  with the Dirichlet boundary condition coupling the two-scales now applying at the external boundary of the micro-cell ( $\partial\mathcal{C}_x$ ). This allows the macroscopic flux  $\mathbf{Q}_a$  to be computed as the average of

---

<sup>2</sup>Note that both sub-domains being connected complicates the model formulation because two equations are now required at the macroscale. The boundary conditions applied on the micro-cells would also need to be modified.

the microscopic fluxes over the micro-cell (16h), bypassing the need for the effective conductivity  $\mathbf{K}_{\text{eff}}$ . Using the same reasoning presented previously for the macroscale model (Section 2.3) the definition of the macroscopic flux  $\mathbf{Q}_a$  must include the contribution of the flux over  $\mathcal{C}_{x,b}$  in addition to  $\mathcal{C}_{x,a}$ . Solving the two-scale model (16) is less expensive than solving the fine-scale model (2) for two main reasons. Firstly, spatial discretization of (16) requires fewer mesh elements/nodes as the micro-cells do not necessarily completely cover the full domain  $\Omega$ . Secondly, EDMM reduces the coupling between discrete unknowns (as evident later in Figure 6, which depicts the Jacobian matrix of the discrete system).

#### 4. Numerical scheme for two-scale computations

In this section, we outline our numerical scheme for implementing DMM (Section 2.4) and EDMM (Section 3) in two spatial dimensions ( $\Omega \subset \mathbb{R}^2$ ). As previously mentioned, our strategy is based on the method by Carr and Turner [4] with two key developments. The first development is to centre the micro-cells around the centroids of each macroscopic element rather than around the macroscopic nodes. This overcomes the issue that occurs at the macroscopic boundary nodes where part of the micro-cell incorrectly lies outside the domain  $\Omega$ . The second development is to supply the value for the microscale Dirichlet boundary conditions (14c) and (16f) by constructing an interpolating function of the macroscopic field  $U_a$ . This approach more accurately captures the direction of the transport/flow in the micro-cell and ensures the microscopic field ( $u_b$ ) is suitably bounded by the macroscopic field ( $U_a$ ). This new approach is a significant step forward on the scheme proposed by Carr and Turner [4], which was valid only for small micro-cells since physically reasonable values of the microscopic field were not guaranteed.

With the above positioning of the micro-cells, the new numerical scheme permits both two-scale models (DMM and EDMM) to be correctly validated against the fine-scale model (Section 2.1) for a periodic medium (e.g., an  $n \times n$  arrangement of micro-cells). This is achieved using an  $n \times n$  macroscopic grid so that the location and geometry of the micro-cells coincide precisely with the heterogeneous geometry of the full domain  $\Omega$ . Previously in the literature, such comparisons against the fine-scale model have involved an inconsistency between the macroscopic grid and micro-cell configuration. For example, Szymkiewicz [29] compared the two-scale model computed on a  $40 \times 40$  macroscopic grid to the fine-scale model computed on a  $10 \times 10$  arrangement of micro-cells. In this case, there is an inconsistency present since the macroscopic grid spacing is smaller than the width of the micro-cells resulting in a higher number of micro-cells for the two-scale model than the fine-scale model.

The two-scale numerical scheme begins by generating a macroscopic mesh over the domain  $\Omega$  (see Figures 3 and 4). The mesh generated should be significantly more coarse than the mesh required to solve the fine-scale model (2). An individual micro-cell is then assigned to each of the macroscopic elements  $i = 1, \dots, m$ . For macroscopic element  $i$  we let  $\mathcal{C}_i$  denote its corresponding micro-cell (with external boundary  $\partial\mathcal{C}_i$ ) and assume that  $\mathcal{C}_i$  is centered at the centroid of the element. The micro-cells resolve the fine-scale geometry within the small domains: the components of  $\mathcal{C}_i$  corresponding to the sub-domains  $\Omega_a$  and  $\Omega_b$  are denoted by  $\mathcal{C}_{i,a}$  and  $\mathcal{C}_{i,b}$ , respectively while  $\Gamma_i$  is the interface between the two sub-domains within  $\mathcal{C}_i$ . In total  $m$  micro-cell problems are defined: on each cell  $\mathcal{C}_i$  a separate micro-cell problem (equations 14b and 14c for DMM and equations 16b–16f for EDMM)

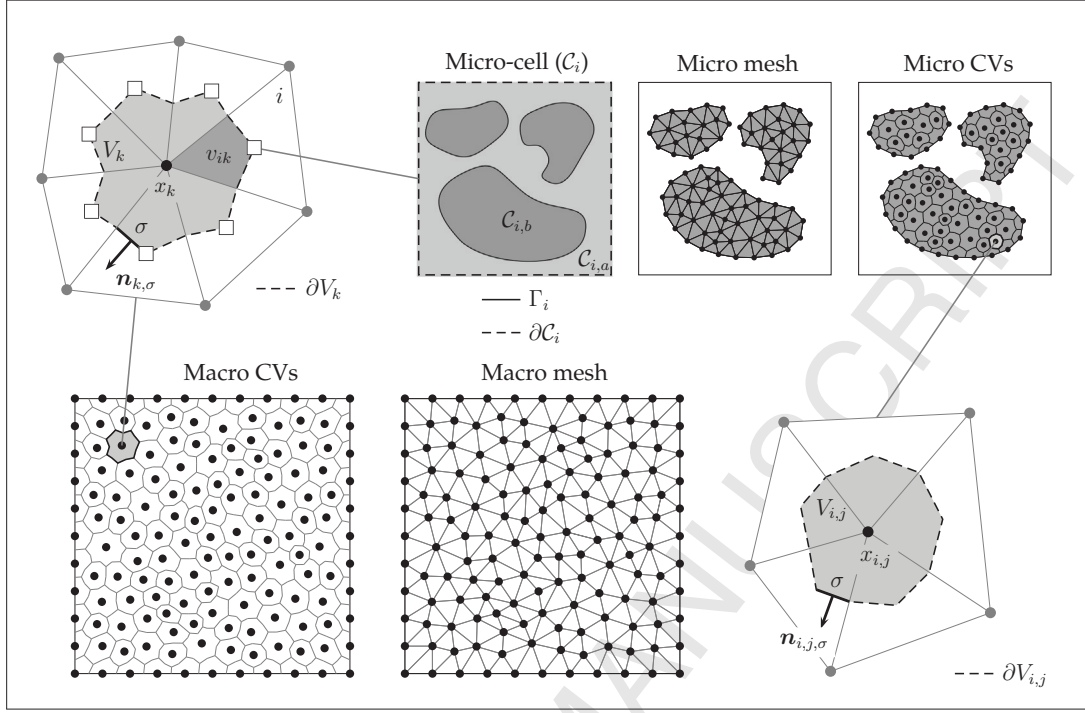


Figure 3: Control Volume Finite Element Formulation for DMM.

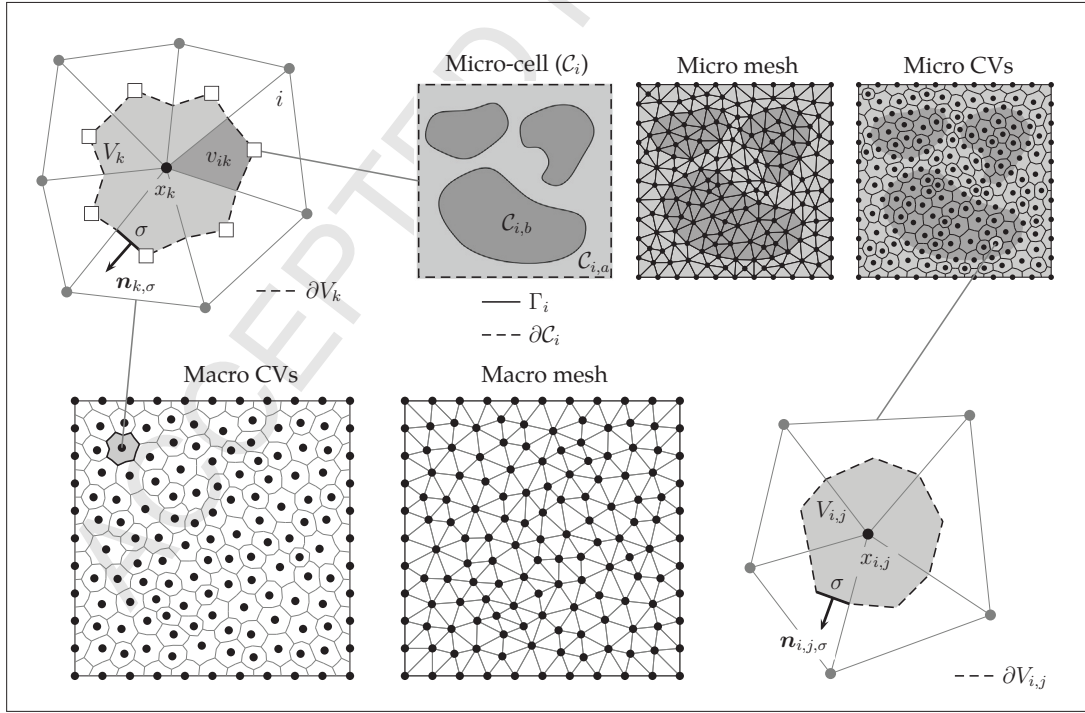


Figure 4: Control Volume Finite Element Formulation for EDMM.

is specified with the variables  $u_{a,i}$  and  $u_{b,i}$  used to denote the microscopic fields within  $\mathcal{C}_{i,a}$  and  $\mathcal{C}_{i,b}$ , respectively.

At both scales, spatial discretization of the governing equations is carried out using a vertex-centered control volume finite element method: discrete unknowns are positioned at the vertices in the mesh, control volumes are formed around each node by connecting the centroid of each element to the midpoint of its edges (see Figures 3 and 4) and finite element shape functions are used for flux approximation at control volume edges. We allow for either triangular or quadrilateral elements at both scales using the usual  $\mathcal{P}_1$  linear and  $\mathcal{Q}_1$  bilinear shape functions, respectively.

#### 4.1. Macroscale equation

Let  $V_k$  be the control volume associated with an arbitrary macroscopic node  $k$  located at the point  $x_k$  (see Figures 3 and 4). After integrating the macroscopic equation (equation 14a for DMM and equation 16a for EDMM) over the control volume, we obtain the following discrete analog:

$$\varepsilon_a \frac{d\Psi_{a,k}}{dt} + \frac{1}{|V_k|} \sum_{\sigma \subset \partial V_k} F_{k,\sigma} = S_k, \quad (17)$$

where  $\Psi_{a,k} = f_a(U_{a,k})$ ,  $U_{a,k}$  denotes the macroscopic discrete unknown at node  $k$ ,  $|V_k|$  is the area of  $V_k$ , and  $S_k$  is the source term associated with node  $k$ , which is recovered from the solution of the  $m$  micro-cell problems (see Section 4.5). Define the component of the macroscopic flux exiting the control volume  $V_k$  through the edge  $\sigma$  by:

$$Q_{k,\sigma} = \int_{\sigma} \mathbf{Q}_a \cdot \mathbf{n}_{k,\sigma} ds, \quad (18)$$

where  $\mathbf{n}_{k,\sigma}$  is the unit vector normal to edge  $\sigma$  directed outward from control volume  $V_k$  (see Figures 3 and 4). In equation (17) the sum is taken over the edges that comprise the control volume boundary  $\partial V_k$  where  $F_{k,\sigma}$  denotes the discrete form of  $Q_{k,\sigma}$  (18). Computation of  $F_{k,\sigma}$  is addressed later in Section 4.3.

#### 4.2. Microscale equation

Let  $V_{i,j}$  denote the control volume corresponding to an arbitrary microscopic node  $j$  within micro-cell  $\mathcal{C}_i$  (see Figures 3 and 4). The following discretisation of the microscopic equation (equation 14b for DMM and 16b for EDMM) over  $V_{i,j}$  is obtained:

$$\frac{d\psi_{b,i,j}}{dt} + \frac{1}{|V_{i,j}|} \sum_{\sigma \subset \partial V_{i,j}} F_{i,j,\sigma} = 0, \quad i = 1, \dots, m, \quad (19)$$

where  $\psi_{b,i,j} = f_b(u_{b,i,j})$ ,  $u_{b,i,j}$  denotes the microscopic discrete unknown at node  $j$  (micro-cell  $\mathcal{C}_i$ ) and time  $t$ ,  $|V_{i,j}|$  is the area of  $V_{i,j}$ , and the sum is taken over the edges that comprise the control volume boundary  $\partial V_{i,j}$ . Define the component of the microscopic flux exiting the control volume  $V_{i,j}$  through the edge  $\sigma$  by:

$$q_{i,j,\sigma} = \begin{cases} \int_{\sigma} \mathbf{q}_a \cdot \mathbf{n}_{i,j,\sigma} ds & \text{if } \sigma \subset \mathcal{C}_{i,a} \\ \int_{\sigma} \mathbf{q}_b \cdot \mathbf{n}_{i,j,\sigma} ds & \text{if } \sigma \subset \mathcal{C}_{i,b} \end{cases} \quad (20)$$

where  $\mathbf{n}_{i,j,\sigma}$  is the unit vector normal to edge  $\sigma$  directed outward from control volume  $V_{i,j}$ . The microscopic numerical flux  $F_{i,j,\sigma}$  appearing in equation (19) denotes the discrete form of  $q_{i,j,\sigma}$  computed by applying midpoint quadrature to the integrals in equation (20). Gradient and conductivity terms are then evaluated at the midpoint of an edge  $\sigma$  using finite element shape functions.

#### 4.3. Computation of the macroscopic flux

The macroscopic numerical flux  $F_{k,\sigma}$  appearing in the macroscopic control volume equation (17) is computed by applying midpoint quadrature to the integral (18):

$$F_{k,\sigma} = (\mathbf{Q}_{a,\sigma} \cdot \mathbf{n}_{k,\sigma}) |\sigma|,$$

where  $\mathbf{Q}_{a,\sigma}$  is an approximation to the flux vector  $\mathbf{Q}_a$  at the midpoint of edge  $\sigma$  and  $|\sigma|$  is the length of  $\sigma$ . For DMM, to compute  $\mathbf{Q}_{a,\sigma}$ , gradient and conductivity terms (15) are evaluated at the midpoint of  $\sigma$  using finite element shape functions. For EDMM,  $\mathbf{Q}_{a,\sigma}$  is defined in terms of the microscopic fluxes via an approximation to the definition (16h):

$$\mathbf{Q}_{a,\sigma} = \frac{1}{|\mathcal{C}_i|} \left( \sum_{e \in \mathcal{C}_{i,a}} \mathbf{q}_{a,e} |e| + \sum_{e \in \mathcal{C}_{i,b}} \mathbf{q}_{b,e} |e| \right). \quad (21)$$

In this equation, the sums are taken over the elements that comprise  $\mathcal{C}_{i,a}$  and  $\mathcal{C}_{i,b}$  and  $|e|$  is the area of element  $e$ . The vectors  $\mathbf{q}_{a,e}$  and  $\mathbf{q}_{b,e}$  are approximations to the flux vectors  $\mathbf{q}_a$  and  $\mathbf{q}_e$  at the centroid of element  $e$ : gradient and conductivity terms are evaluated at the centroid of element  $e$  using finite element shape functions.

#### 4.4. Microscopic boundary condition

Recall, that the micro-cell problems include a Dirichlet boundary condition (equation 14c for DMM and equation 16f for EDMM) relating the microscopic fields ( $u_{b,i}$  for DMM,  $u_{a,i}$  and  $u_{b,i}$  for EDMM,  $i = 1, \dots, m$ ) to the macroscopic unknowns ( $U_{a,k}$ ). For DMM, when the micro-cells are located at the macroscopic nodes, the usual approach is to use a uniform value along the interface ( $\Gamma_i$ ) equal to the value at the macroscopic node. Figure 5 provides a simulation of Richards' equation flow in a standalone micro-cell comprising a square inclusion, where the conductivity is 100 times smaller in the inclusions than in the surrounding medium. This figure demonstrates that the assumption of a uniform Dirichlet condition along the inclusion boundary is violated. In previous work [4], we positioned the micro-cells at the macroscopic nodes and let the microscopic field  $u_{b,i}$  vary linearly along  $\Gamma_i$  according to an approximation of the macroscopic gradient at the macroscopic node. This method, however, is restricted to very small-cells since physically-reasonable values of the solution were not guaranteed. In this work, with the micro-cells defined element-wise (see Figures 3 and 4), we propose to use the following interpolant of the macroscopic field:

$$u_{b,i,j} = \sum_{k \in \mathcal{V}_i} U_{a,k} N_k(x_{i,j}), \quad x_{i,j} \in \Gamma_i, \quad (22)$$

to compute the values along the boundary ( $x_{i,j} \in \Gamma_i$  for DMM and  $x_{i,j} \in \partial \mathcal{C}_i$  for EDMM), where  $\mathcal{V}_i$  is the set of vertices for element  $i$  and  $N_k(x)$  is the usual  $\mathcal{P}_1$  linear (triangular elements) or  $\mathcal{Q}_1$  bilinear (quadrilateral elements) shape function that takes the value one at vertex  $k$  and zero at all other vertices of element  $i$ . This approach captures the effect of the macroscopic gradient whilst suitably bounding the microscopic field within the micro-cell  $\mathcal{C}_i$  by the macroscopic nodal values ( $U_{a,k}$ ).

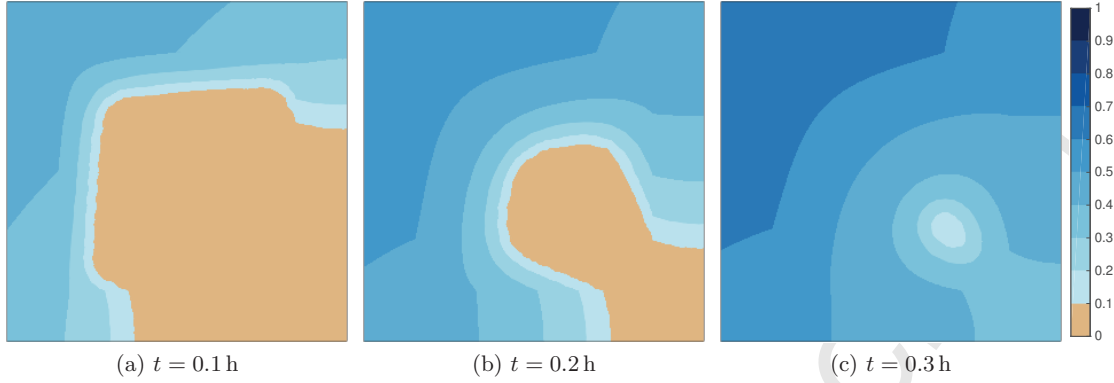


Figure 5: Saturation contours describing water flow in a micro-cell  $\mathcal{C}_x$  containing a single square inclusion of low conductivity ( $K_b/K_a = 10^{-2}$ ) demonstrating the non-uniform value of the microscopic field along the interface  $\Gamma_x$  and external boundary  $\partial\mathcal{C}_x$ . Boundary conditions impose a constant influx of water along the left and top boundaries while zero flux and free drainage conditions are specified along the bottom and right boundaries, respectively.

#### 4.5. Computation of the source term

The source term  $S_k$  that appears in the discrete macroscopic equation (17), quantifies the exchange of heat/fluid/mass between the two materials within control volume  $V_k$  and is recovered from the microscopic field. For micro-cell  $\mathcal{C}_i$ , the source term (equation (14d) and (16g)) is computed numerically as:

$$S_i = \frac{1}{|\mathcal{C}_i|} \sum_{\sigma \in \Gamma_i} B_{i,\sigma}, \quad (23)$$

where the sum is taken over the edges that comprise the interface  $\Gamma_i$ . Define the component of the microscopic flux exiting the inclusions through an interface edge  $\sigma$  by

$$q_{i,\sigma} = \int_{\sigma} \mathbf{q}_b \cdot \mathbf{n}_{\sigma} ds, \quad (24)$$

where  $\mathbf{n}_{\sigma}$  is the unit vector normal to edge  $\sigma$  pointing outwards from  $\mathcal{C}_{i,b}$ . In equation (23),  $B_{i,\sigma}$  denotes the discrete form of  $q_{i,\sigma}$  computed by approximating the integral (24) using a midpoint quadrature rule with gradient and conductivity terms evaluated at the midpoint of edge  $\sigma$  using finite element shape functions. The macroscopic source term at node  $k$  is then computed using the area-weighted average:

$$S_k = \frac{1}{|V_k|} \sum_{i \in E_k} S_i |v_{ik}|, \quad (25)$$

where  $E_k$  denotes the set of elements that contain  $k$  as a vertex and  $v_{ik}$  is the macroscopic sub-control volume representing the intersection of macroscopic element  $i$  and macroscopic control volume  $V_k$  (see Figures 3 and 4).



#### 4.6. Time stepping

The discrete equations (17) and (19) are assembled for all the macroscopic and microscopic nodes (not including those nodes located on boundaries where Dirichlet conditions are imposed) into a single system of coupled ordinary differential equations that can be expressed in the form:

$$\frac{d\mathbf{\Psi}}{dt} = \mathbf{g}(\mathbf{\Psi}), \quad \mathbf{\Psi}(0) = \mathbf{\Psi}_0, \quad (26)$$

where  $\mathbf{\Psi}$  is the solution vector at time  $t$  and  $\mathbf{g}$  is a non-linear vector-valued function of  $\mathbf{\Psi}$  containing the spatial discretization terms on the right-hand sides of equations (17) and (19). Within the vector  $\mathbf{\Psi}$  the macroscopic discrete unknowns  $\Psi_{a,k}$  are listed first, followed by the microscopic discrete unknowns  $\Psi_{b,i,j}$  grouped according to the  $m$  micro-cells. As an example, Figure 6 depicts the complex structure of the Jacobian matrix of  $\mathbf{g}(\mathbf{\Psi})$  for a very coarse macroscopic mesh consisting of 60 triangular elements. The first block along the diagonal corresponds to the macroscopic nodes and the remaining 60 blocks correspond to each of the 60 micro-cell problems. The off-block-diagonal entries are due to the coupling between scales: the entries above the block diagonal are due to the macroscopic source term (25), which is a function of the microscopic fields in the micro-cells, and the entries below the block diagonal are a result of the microscopic boundary condition (equation 14c for DMM and equation 16f for EDMM), which is a function of the macroscopic field.

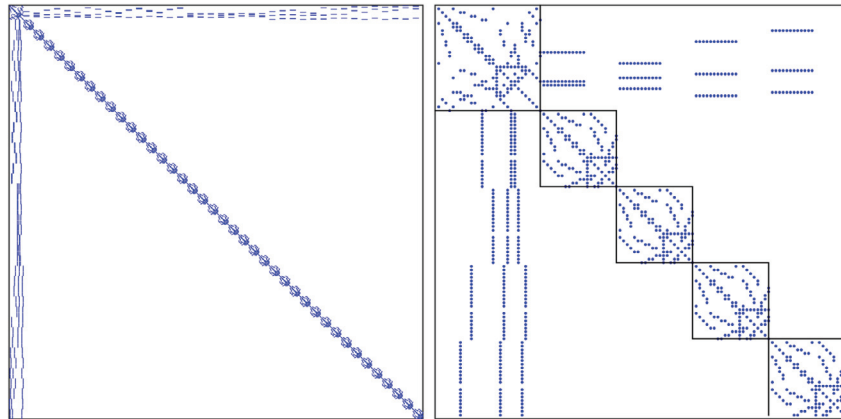


Figure 6: Example Jacobian structure of the vector-valued function  $g(u)$  in the ODE system (26). Full Jacobian matrix shown on the left and a zoomed in view of the first five blocks on the right.

The initial value problem (26) is solved numerically using the exponential Rosenbrock-Euler method [5, 6, 13], which relates the solution at  $t = t_{n+1}$  ( $\mathbf{\Psi}_{n+1}$ ) to the solution at  $t = t_n$  ( $\mathbf{\Psi}_n$ ) via the time-stepping formula:

$$\mathbf{\Psi}_{n+1} = \mathbf{\Psi}_n + \tau_n \varphi(\tau_n \mathbf{J}_g(\mathbf{\Psi}_n)) \mathbf{g}(\mathbf{\Psi}_n), \quad (27)$$

where  $\tau_n = t_{n+1} - t_n$  is the stepsize,  $\mathbf{J}_g$  is the square Jacobian matrix of  $\mathbf{g}(\mathbf{\Psi})$  and  $\varphi$  is a matrix function defined as  $\varphi(\mathbf{A}) = \mathbf{A}^{-1}(e^{\mathbf{A}} - \mathbf{I})$ . This scheme is attractive from a computational viewpoint because it has excellent stability properties, it is second-order accurate in time (one order higher than the implicit/backward Euler method) [5], and it does not involve the solution of a linear or nonlinear system of equations at each time step.

The matrix-function vector product in equation (27) is computed using the Krylov subspace approximation:

$$\varphi(\tau_n \mathbf{J}_g(\Psi_n)) \mathbf{g}(\Psi_n) \simeq \beta_0 \mathbf{V}_m \varphi(\tau_n \mathbf{H}_m) \mathbf{e}_1, \quad (28)$$

where the columns of  $\mathbf{V}_m$  form an orthonormal basis for the Krylov subspace  $\mathcal{K}_m(\mathbf{J}_g(\Psi_n), \mathbf{g}(\Psi_n))$  and  $\mathbf{H}_m = \mathbf{V}_m^T \mathbf{J}_g(\Psi_n) \mathbf{V}_m$  is the usual  $m \times m$  upper Hessenberg matrix arising in Arnoldi's iteration (see, e.g., [5, §5.1]). The matrix  $\mathbf{H}_m$  is very small compared to  $\mathbf{J}_g$ , with computation of  $\varphi(\tau_n \mathbf{H}_m)$  carried out using Padé approximation [5, 6]. This Krylov subspace method does not require preconditioning since it converges rapidly for the given  $\varphi$ -function. As a result, the time stepping procedure requires only matrix-vector products with the Jacobian matrix (when generating an orthonormal basis for the Krylov subspace method using Arnoldi's iteration), which can be approximated accurately and efficiently using difference quotients involving evaluations of  $\mathbf{g}(\Psi)$  (see, e.g., [6, Eq. 30]). In summary, by using the exponential Rosenbrock-Euler method we completely avoid having to generate or store the complex Jacobian matrix (Figure 6).

The size of the time step  $\tau_n$  is adaptively controlled throughout the time integration according to the variable stepsize algorithm proposed by Carr et al. [5]. At the beginning of each time step, an attempt is made to advance the solution by a candidate stepsize. If the Krylov subspace iterations fail to converge, the stepsize is repeatedly reduced until convergence is attained. Otherwise, the local error of the computed solution is estimated and assessed against an error criterion that depends on the absolute and relative error tolerances supplied by the user. If successful, the solution is accepted and a new candidate stepsize for the next time step proposed. Otherwise the stepsize is reduced and the process repeated. The local error is estimated as the difference between  $\Psi_{n+1}$  (27) and a second-approximate solution  $\Psi_{n+1}^{(2)}$  computed using a two-step exponential Rosenbrock-Euler scheme with half-sized time steps. The reader is referred to [5, §5.2] for the complete details.

#### 4.7. Code implementation

We have implemented the two-scale numerical scheme discussed in the previous sections in a computational code developed in C++. Linear algebra operations, such as those required when generating an orthonormal basis for the Krylov subspace (Arnoldi's iteration), are carried out using BLAS and LAPACK subroutines.

The computational cost of the code is dominated by evaluations of the vector-valued function  $\mathbf{g}(\Psi)$  that appears in the ODE system (26). These evaluations are themselves dominated by a loop over the number of macroscopic elements ( $i = 1, \dots, m$ ). Iteration  $i$  of this loop involves the following sub-tasks:

- (i) Compute the macroscopic numerical fluxes  $F_{k,\sigma}$  for edges  $\sigma$  located in element  $i$  and assemble these according to the macroscopic discrete equations (17).
- (ii) Compute the source  $S_i$  (23) for element  $i$  and distribute its value according to the macroscopic discrete equations (17) via equation (25).
- (iii) A loop over the number of elements within the microscopic mesh associated with micro-cell  $C_i$ , which computes the microscopic numerical fluxes  $F_{i,j,\sigma}$  and assembles them according to the microscopic discrete equations (19). For EDMM this step also involves computing the macroscopic flux according to equation (21).

To speed up the simulations, we have implemented the loop over the number of macroscopic elements in parallel using OpenMP. To avoid race conditions, where entries of the one-dimensional array representing the right-hand side vector  $\mathbf{g}(\Psi)$  (equation 26) are erroneously accessed and updated simultaneously, the array is promoted to a multidimensional array indexed by the number of threads. All simulation results reported in the next section were obtained using the high performance computing facilities at Queensland University of Technology (QUT). The code was compiled using `icpc` with `-O2` optimization and we used the BLAS and LAPACK subroutines from the Intel Math Kernel Library (MKL) (all found within Intel Composer XE 2013.3.163). All finite element meshes were generated using GMSH [12].

## 5. Results and discussion

In this section, we assess the performance of the DMM and EDMM two-scale models (Sections 2.4 and 3) against the classical macroscopic model (Section 2.3) and fine-scale model (Section 2.1). All comparisons are performed using a numerical solution to the fine-scale model as a benchmark. To remain consistent, numerical solutions to the macroscopic model and fine-scale model were computed using equivalent spatial and temporal discretisations (as discussed in Sections 4.1 and 4.6) with computation and assembly of the fluxes also carried out in parallel using OpenMP.

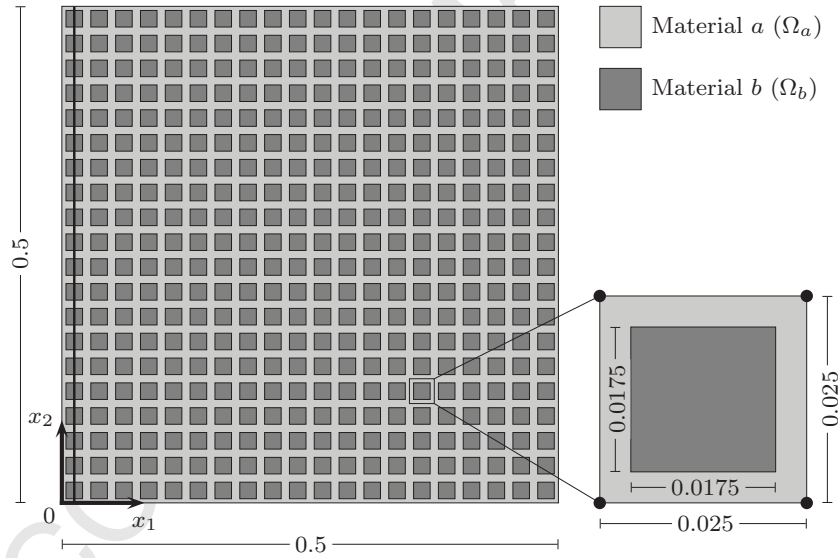


Figure 7: Schematic representation of the domain  $\Omega$  for both test cases. The diagram depicts the line used in the Tables 1 and 2 and Figures 8 and 11 is shown and the bullets ( $\bullet$ ) identify the locations of the macroscopic nodes.

In both test cases, we consider the binary domain depicted in Figure 7. The domain  $\Omega$  is a square of length 0.5 ( $\Omega = [0, 0.5] \times [0, 0.5]$ ) consisting of a  $20 \times 20$  array of square inclusions, each with length 0.0175. A structured macroscopic mesh comprising of 400 quadrilateral elements ( $20 \times 20$  grid with equal node spacing of 0.025) is used for both the macroscopic and two-scale models. This choice for the macroscopic mesh ensures that the micro-cells, which are centered at the centroid of each

macroscopic element (see Figures 3 and 4), coincide precisely with the heterogeneous geometry of the domain.

For the above configuration, it is possible to compare the two-scale solutions to “exact” solutions obtained by solving the fine-scale model on the full heterogeneous geometry. Since the micro-cell size is equal to the size of the macroscopic element, the two-scale solutions provide an approximation to the fine-scale solution across the full domain  $\Omega$ : solution fields for the two-scale models can be produced in the full heterogeneous geometry by overlaying the macroscopic field with the field in each micro-cell.

The two test cases are described as follows:

- (i) Case A solves the linear heat equation on  $\Omega$ :

$$\begin{aligned} \frac{\partial u_a}{\partial t} + \nabla \cdot (-K_a \nabla u_a) &= 0 \quad \text{in } \Omega_a \\ \frac{\partial u_b}{\partial t} + \nabla \cdot (-K_b \nabla u_b) &= 0 \quad \text{in } \Omega_b \\ u_a &= u_b \quad \text{on } \Gamma \\ -K_a \nabla u_a \cdot \mathbf{n} &= -K_b \nabla u_b \cdot \mathbf{n} \quad \text{on } \Gamma \end{aligned}$$

where  $u$  is the dimensionless temperature and  $K$  is the dimensionless thermal diffusivity. A Dirichlet boundary condition ( $u_a = 1$ ) is imposed at the top boundary ( $y = 0.5$ ) while all remaining boundaries are taken as no flux. At  $t = 0$ ,  $u_0(x) = 0$  and the simulations are run until  $t = 0.6$ . The diffusivity  $K_a = 1$  while different values for  $K_b$  are investigated.

- (ii) Case B solves the nonlinear unsaturated Richards’ equation on  $\Omega$  (with the given dimensions in metres):

$$\begin{aligned} \frac{\partial \theta_a}{\partial t} + \nabla \cdot (-K_a(h_a) \nabla (h_a + x_2)) &= 0 \quad \text{in } \Omega_a \\ \frac{\partial \theta_b}{\partial t} + \nabla \cdot (-K_b(h_b) \nabla (h_b + x_2)) &= 0 \quad \text{in } \Omega_b \\ h_a &= h_b \quad \text{on } \Gamma \\ -K_a(h_a) \nabla (h_a + x_2) \cdot \mathbf{n} &= -K_b(h_b) \nabla (h_b + x_2) \cdot \mathbf{n} \quad \text{on } \Gamma \end{aligned}$$

where  $\theta$  is the moisture content,  $K$  is the hydraulic conductivity,  $h$  is the pressure head and gravity acts in the vertical direction (negative  $x_2$ ) direction. This equation is often used to model the flow of water through unsaturated soils and provides a challenging problem due to its highly nonlinear constitutive laws.

To close the model, we use the van Genuchten-Maulem relationships [18, 30], which express the moisture content and hydraulic conductivity in terms of the capillary pressure head:

$$\begin{aligned} \theta(h) &= \theta_{\text{res}} + (\theta_{\text{sat}} - \theta_{\text{res}}) S_e(h), \\ K(h) &= K_{\text{sat}} S_e(h) \left[ 1 - (1 - S_e(h))^{1/m} \right]^m. \end{aligned}$$

where  $S_e$  is the effective saturation

$$S_e(h) = [1 + |\alpha h|^n]^{-m},$$

$K_{\text{sat}}$  is the saturated hydraulic conductivity [ $LT^{-1}$ ]  $\theta_{\text{res}}$  [–] is the residual moisture content,  $\theta_{\text{sat}}$  [–] is the saturated moisture content and  $\alpha$  [ $L^{-1}$ ],  $n$  [–] and  $m = 1 - 1/n$  [–] are empirical parameters. For the problem considered here, we assume that both materials take the form of a typical sandy loam [27]:  $\theta_{\text{res}} = 0.058$ ,  $\theta_{\text{sat}} = 0.41$ ,  $\alpha = 7.3 \text{ m}^{-1}$  and  $n = 1.89$  in both  $\Omega_a$  and  $\Omega_b$  with  $K_{\text{sat}} = 4.4 \text{ m h}^{-2}$  in  $\Omega_a$ . Several values for  $K_{\text{sat}}$  in  $\Omega_b$  are tested corresponding to the conductivity ratios  $K_b/K_a = 1, 10^{-1}, 10^{-2}, \dots, 10^{-4}$ .

Water infiltrates into the domain through a 0.2 m wide (eight micro-cells wide) section along the left-hand side of the top boundary ( $0 \leq x \leq 0.2$  and  $y = 0.5$ ) at a constant rate of  $q_b = -0.003 \text{ m h}^{-1}$ . Free drainage is imposed at the bottom boundary ( $y = 0$ ) while all remaining boundaries are considered impermeable. Initially, the capillary pressure head field is flat ( $h_0(x) = -20 \text{ m}$ ), which corresponds to dry conditions with an initial effective saturation of 0.0118. Each simulation is run until  $t = 500 \text{ h}$ .

As a measure of the accuracy of the macroscopic and two-scale models we record the mean squared error of each solution:

$$\text{ERROR} = \frac{1}{N} \sum_{i=1}^N (\hat{u}_i - u_i)^2,$$

where  $u$  is the fine-scale solution and  $\hat{u}$  is the approximate solution (macroscopic, DMM or EDMM solution). The error is computed using  $N$  uniformly distributed points along the line  $x_1 = 0.0125$ , which passes through the centre of the first column of micro-cells in Figure 7. The error is computed at a small chosen value of time at which the fine-scale field possess a large gradient near  $x_2 = 0.5$  and rapid variation along the line  $x_1 = 0.0125$  due to the inclusions. The wall time, mean time step size and mean Krylov subspace dimension (to compute the matrix-vector product given in equation 27) over the entire length of the simulation are recorded to assess the computational cost of each model. The calculations required to compute the effective conductivity  $\mathbf{K}_{\text{eff}}$  for the macroscopic model and DMM were carried out separately in MATLAB and hence were not included in the aforementioned wall time.

The total number of unknowns is equal to 441, 47641, 87641 and 104860 for the macroscopic, DMM, EDMM and fine-scale models, respectively. For both test cases and both models the simulations are carried out with an initial time step of  $10^{-6} \text{ h}$  and absolute and relative time integration error tolerances of  $10^{-5}$  (within the exponential Rosenbrock-Euler method). Maximum allowable time step sizes of  $10^{-2}$  and 1 h are set for Case A and Case B, respectively.

### 5.1. Case A

Simulation results for Case A are given in Figure 8. These figures depict a slice of the two-dimensional solution field at two points in time ( $t = 0.01$  and  $t = 0.3$ ), plotting the solution along the line  $x_1 = 0.0125$ , which passes through the center of the first column of micro-cells (see Figure 7). In addition to the solution fields arising from the fine-scale, macroscopic and two-scale (DMM and EDMM) models, we include a smoothed fine-scale field that profiles the average (in each micro-cell located in the first column) of the fine-scale solution along the line  $x_1 = 0.0125$ . Note that for this test problem, the solution fields are the same within each column of micro-cells due to the boundary conditions, so identical behavior is observed in the other columns. Starting with the

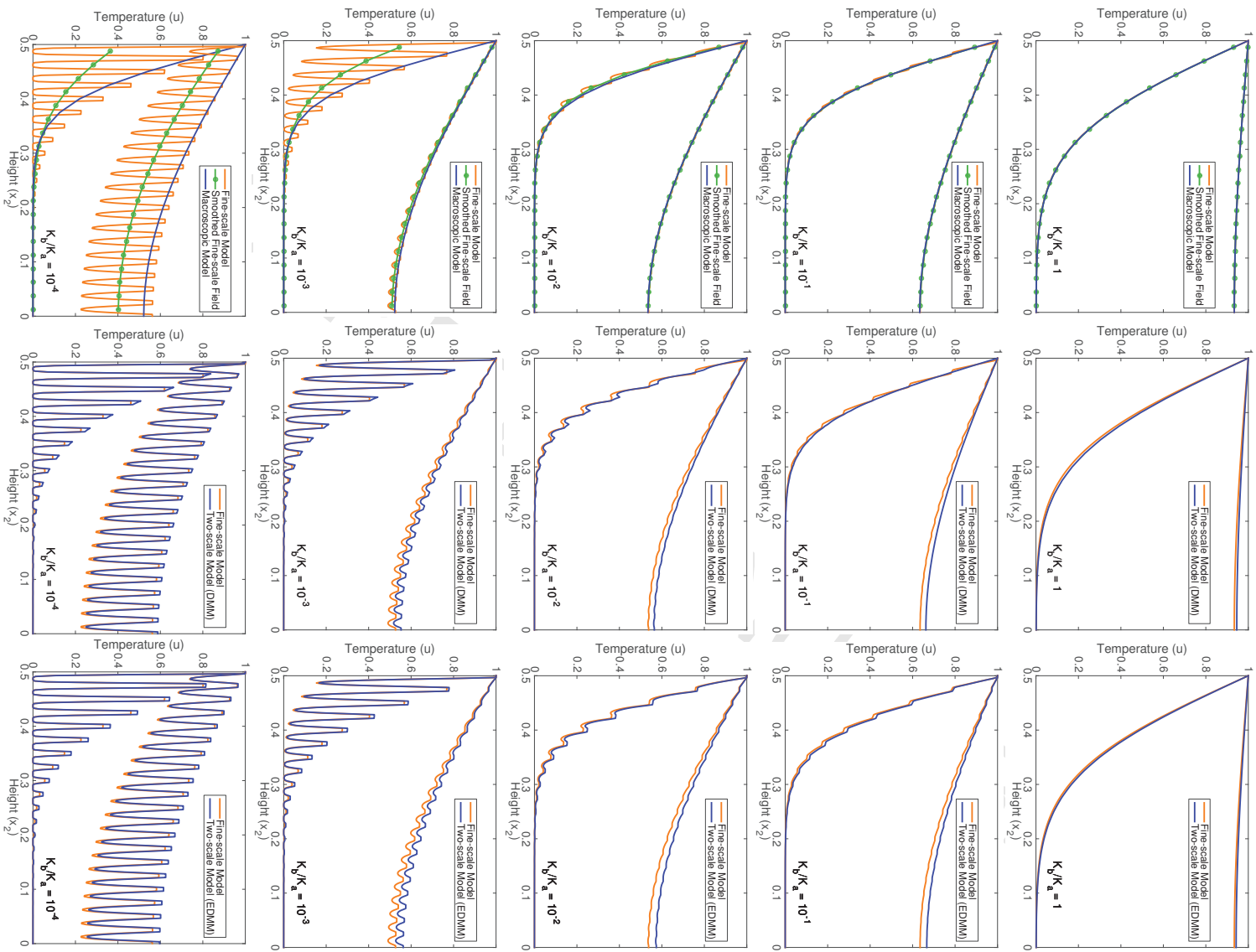


Figure 8: Solution profiles for Case A: plot of the temperature through the centre of the first column of micro-cells (along the line  $x_1 = 0.0125$ ) at  $t = 0.01$  (lower curves) and  $t = 0.3$  (higher curves).

homogeneous problem ( $K_b/K_a = 1$ ), each row of figures successively decreases the diffusivity in  $K_b$  by a factor of 10.

An immediate observation is the huge impact of decreasing the diffusivity ratio on the fine-scale solution and the ability of only the two-scale models (DMM and EDMM) to capture these fine-scale features in the solution. For the homogeneous problem, the macroscopic and fine-scale models are equivalent (the effective diffusivity  $\mathbf{K}_{\text{eff}} = K_a = K_b$ ), which explains why the macroscopic and fine-scale solutions are perfectly aligned visually<sup>3</sup>. On the other hand, as expected, the two-scale solutions (DMM and EDMM) do not achieve perfect alignment for the homogeneous problem, however, only small deviations from the fine-scale solution can be observed. Upon closer inspection of the figures, we see that EDMM performs better than DMM, which is a direct result of the assumption of equilibrium in  $\mathcal{C}_{x,a}$  (part of the micro-cell occupied by material  $a$ ) for DMM, an assumption which is absent from EDMM (see the third point listed at the beginning of Section 3).

Several other interesting observations can be drawn from Figure 8. For  $K_b/K_a = 10^{-1}$ , we start to see some small oscillations in the fine-scale solution due to the heterogeneity. Only EDMM is able to capture these small features in the solution with both the macroscopic and DMM solutions remaining smooth. Another observation is that the macroscopic solution is a poor approximation to the smoothed/averaged fine-scale solution, instead favouring the solution in the connected material ( $\Omega_a$ ). The macroscopic solution also tends to slightly underestimate the vertical flow (flow in negative  $x_2$  direction) while both DMM and EDMM slightly overestimate the flow in this direction. Finally, after careful inspection of the figures, we see that EDMM has the advantage that it captures the correct solution gradient in the connected material  $a$  (i.e., the slopes of the peaks in the solution) while DMM fails to do this. This is particularly evident in the last two rows of figures ( $K_b/K_a = 10^{-3}, 10^{-4}$ ).

Simulations statistics for Case A are given in Table 1. The error measurements confirm the observations drawn from Figure 8: the error in the macroscopic solution of the homogeneous problem is small but not zero, the macroscopic model is marginally more accurate for large values of the diffusivity ratio (smaller contrast between diffusivities), the two-scale models are significantly more accurate than the macroscopic model for small values of the diffusivity ratio (large contrast between diffusivities), both DMM and EDMM produce solutions of an equivalent order of accuracy, and the error in the DMM and EDMM solutions are practically independent of the diffusivity ratio. The fine-scale model is significantly more challenging to solve numerically, requiring more computational time, a smaller time step and a larger Krylov subspace dimension to complete the simulation. Overall, DMM requires less computational time than EDMM to advance the solution to the final time. This is partly due to the fewer unknowns required in the DMM formulation (only the part of the micro-cell  $\mathcal{C}_x$  occupied by material  $b$  is meshed). Mostly, however, as is clear from Table 1, this is because DMM requires a smaller average dimension of the Krylov subspace as the diffusivity ratio is decreased, which is a direct result of EDMM meshing the full micro-cell and treating the severe discontinuity in the diffusivity at the interface. We conclude that for the simulations tested, DMM and EDMM produce solutions with an error of the order of between  $10^{-4}$  and  $10^{-5}$  at an average speed up of 54.47 and 4.85 over the fine-scale model.

Now consider Case A with the same  $20 \times 20$  macroscopic grid but a larger  $60 \times 60$  array of inclusions (instead of the  $20 \times 20$  array depicted in Figure 7). This configuration ensures that each macroscopic

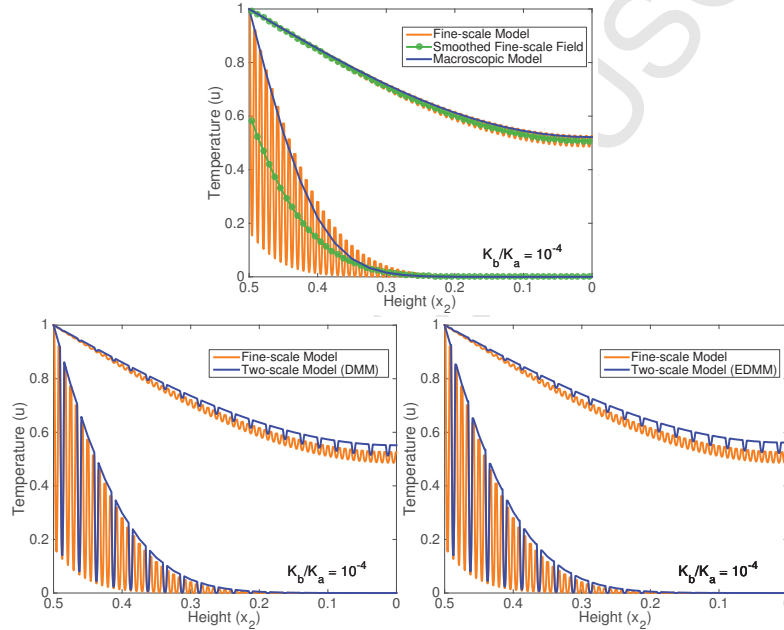
<sup>3</sup>Small discrepancies can be found when observing the numerical values due to the different level of refinement used in both models.



$K_b/K_a$	Model	ERROR	WALLTIME	STEPSIZE	KRYDIM
1	Fine-scale	n/a	03:18	0.0028	58
	Macroscopic	1.14e-06	00:06	0.0041	3
	Two-scale (DMM)	9.13e-05	00:57	0.0040	45
	Two-scale (EDMM)	4.64e-05	01:11	0.0038	50
$10^{-1}$	Fine-scale	n/a	03:20	0.0027	59
	Macroscopic	4.07e-05	00:01	0.0041	3
	Two-scale (DMM)	9.54e-05	00:18	0.0041	19
	Two-scale (EDMM)	7.43e-05	01:20	0.0036	48
$10^{-2}$	Fine-scale	n/a	03:10	0.0024	59
	Macroscopic	3.17e-04	00:01	0.0041	2
	Two-scale (DMM)	1.06e-04	00:09	0.0041	7
	Two-scale (EDMM)	8.10e-05	01:08	0.0038	43
$10^{-3}$	Fine-scale	n/a	04:22	0.0024	60
	Macroscopic	2.15e-02	00:01	0.0041	2
	Two-scale (DMM)	1.07e-04	00:06	0.0041	3
	Two-scale (EDMM)	7.78e-05	01:03	0.0041	32
$10^{-4}$	Fine-scale	n/a	05:27	0.0019	60
	Macroscopic	4.27e-02	00:01	0.0041	2
	Two-scale (DMM)	1.09e-04	00:06	0.0041	4
	Two-scale (EDMM)	1.20e-04	01:03	0.0041	38

Table 1: Simulation statistics for Case A: mean squared error along the line  $x_1 = 0.0125$  at  $t = 0.01$  using the fine-scale solution as the benchmark (ERROR), wall time in minutes and seconds (mm:ss) using a single OpenMP thread (WALLTIME), mean time step size in seconds (STEPSIZE) and mean Krylov subspace dimension (KRYDIM). n/a – not applicable.

element consists of a  $3 \times 3$  sub-grid of inclusions. In the two-scale models (DMM and EDMM), we define the micro-cell around the centre inclusion only (inclusion located in position (2, 2) in the  $3 \times 3$  sub-grid). For example, in the second column of micro-cells the microscale field in the two-scale models is only resolved in the micro-cells located in rows 2, 5,  $\dots$ , 59. This is illustrated in Figure 9, where the solution profiles along the line  $x_1 = 0.0125$  are again shown for  $K_b/K_a = 10^{-4}$ . This “ $60 \times 60$ ” configuration showcases the power of the two-scale modelling approaches. With the number of elements remaining the same in each micro-cell, the number of unknowns in the fine-scale model increases from 104850 to 938292, while the number of unknowns in the macroscopic and two-scale models remain the same (indeed the macroscale model is completely unaffected as the effective conductivity (12) is identical). The end result is that the wall time for the two-scale models remains relatively unchanged while for the fine-scale model the wall time increases from 20 mins to over 6 hours.



$K_b/K_a$	Model	ERROR	WALLTIME	STEPSIZE	KRYDIM
$10^{-4}$	Fine-scale	n/a	06:38:04	0.0005	73
	Macroscopic	2.35e-02	00:00:01	0.0041	2
	Two-scale (DMM)	1.91e-02	00:00:14	0.0041	3
	Two-scale (EDMM)	1.94e-02	00:03:59	0.0040	45

Figure 9: Solution profiles for Case A with a  $60 \times 60$  array of inclusions: plot of the temperature along the line  $x_1 = 0.0125$  (through the centre of the first column of macroscopic elements) at  $t = 0.01$  (lower curves) and  $t = 0.3$  (higher curves). Tabulated is the mean squared error along the line  $x_1 = 0.0125$  at  $t = 0.01$  using the fine-scale solution as the benchmark (ERROR), wall time in minutes and seconds (mm:ss) using 12 OpenMP threads for the fine-scale model and a single OpenMP thread for the macroscopic and two-scale models (WALLTIME), mean time step size in seconds (STEPSIZE) and mean Krylov subspace dimension (KRYDIM). n/a – not applicable.

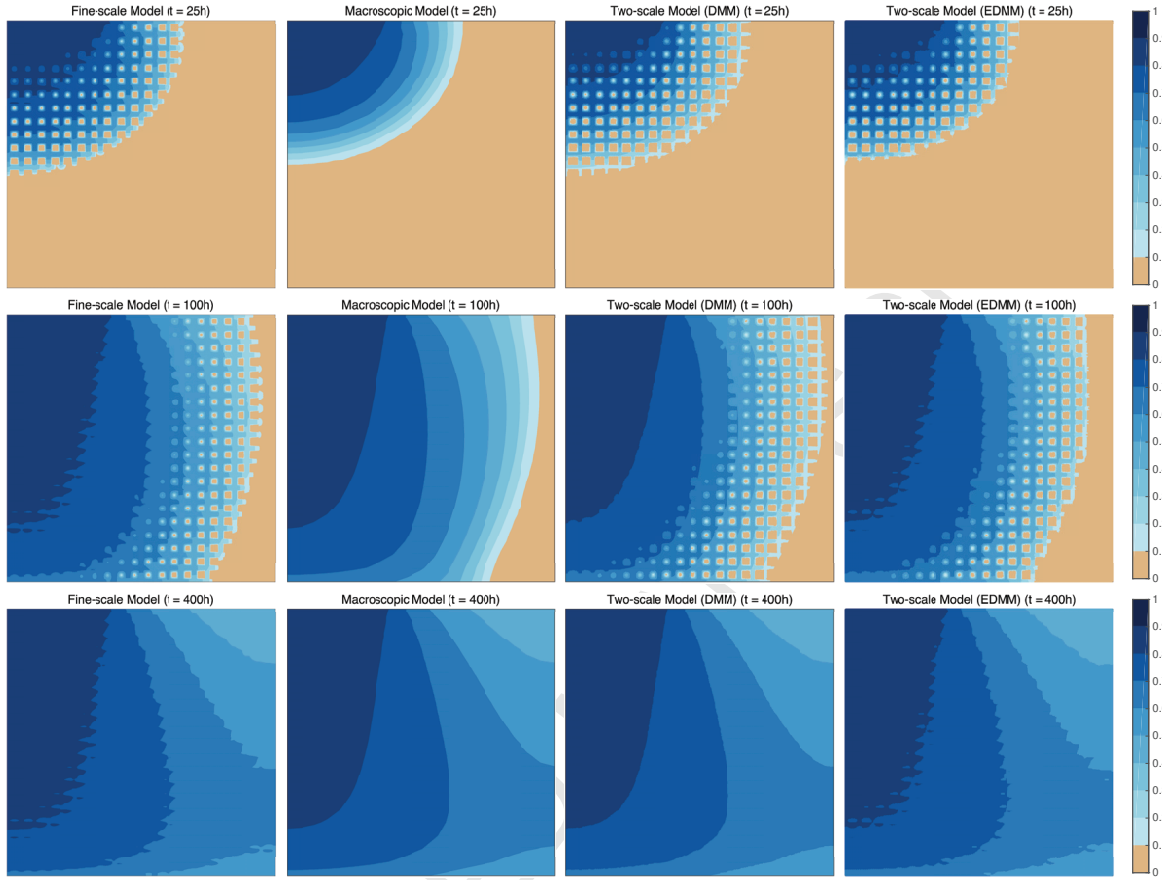


Figure 10: Saturation fields for Case B with  $K_b/K_a = 10^{-3}$ .

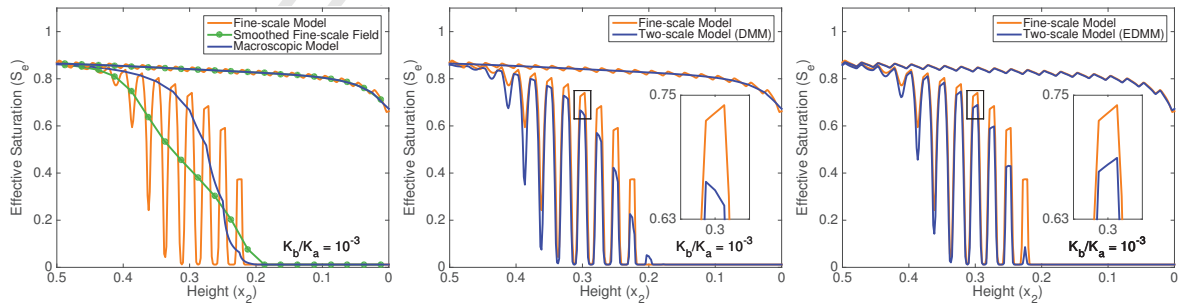


Figure 11: Solution profiles for Case B with  $K_b/K_a = 10^{-3}$ : plot of the effective saturation ( $S_e$ ) through the centre of the first column of micro-cells (along the line  $x_1 = 0.0125$ ) at  $t = 25h$  (lower curves) and  $t = 400h$  (higher curves).

### 5.2. Case B

Saturation fields for Case B are given in Figure 10. These figures plot the two-dimensional solution fields after 25, 100 and 400 hours of infiltration; the latter point at which the solution has attained a steady state. Visually, the two-scale models (DMM and EDMM) are in excellent agreement with the fine-scale model over the entire length of the simulation. The fine-scale model exhibits slow infiltration of water into the inclusions ( $\Omega_b$ ) due to their smaller conductivity. Only the two-scale models are able to capture this behaviour accurately while at the same time accurately capture the field in the connected sub-domain  $\Omega_a$ . Once the inclusions have been infiltrated sufficiently to attain equilibrium with the surrounding field, the contours are very different between both two-scale models. On the one hand, EDMM is able to capture some of the heterogeneous fine-scale features in the solution while DMM only provides a smoothed approximation to the fine-scale contours. This is particularly evident after 400 hours of infiltration when each solution has reached steady state and perhaps even more clearer in Figure 11, which reproduces a plot similar to Figure 8 for Case B, plotting the solution along the line  $x_1 = 0.0125$  at  $t = 400\text{h}$  (and  $t = 25\text{h}$ ).

From Figure 11 we see that the largest errors occur at locations where the fine-scale solution varies most rapidly (i.e., where the saturation contours are closest together). This is mainly tied to the restriction placed on the two-scale model: a  $20 \times 20$  macroscopic mesh must be used to ensure that each micro-cell is associated with one macroscopic element. As a consequence, it is impossible for the macroscopic and two-scale models to perfectly capture the sharp wetting front produced by the fine-scale model (where the pressure head ( $h$ ) varies rapidly), which uses much greater mesh refinement. This leads to larger errors after 25 hours of infiltration where the sharp front is active and smaller errors after 400 hours where it is absent.

Simulation statistics for Case B are given in Table 2. Overall, the solution errors are greater than those for Case A due primarily to the difficulty of resolving the sharp wetting front as mentioned above. In short, the results for Case B agree, for the most part, with the observations reported for Case A. Specifically, the two-scale models are significantly more accurate than the macroscopic model for small values of the conductivity ratio (large contrast between conductivities). Furthermore, the accuracy of the two-scale models (DMM and EDMM) is almost the same across the different conductivity ratios while the accuracy of the macroscopic model declines sharply as the conductivity ratio is decreased. For the simulations tested, on average, DMM is 72.2 times faster than the fine-scale model while an average speedup of 2.93 is recorded for EDMM.

Due to its longer simulation times, Case B provides a good test problem to benchmark the performance of the parallel implementation of the code discussed in Section 4.7. Table 3 records the wall time and speedup factor of the two-scale model (EDMM) for  $K_b/K_a = 10^{-3}$ . These results demonstrate that the speedup is less than ideal (linear) with a factor of 6.69 achieved using 10 OpenMP threads. Nevertheless, parallelisation is helpful, reducing the wall time from over 2 hours and 20 minutes down to less than 22 minutes.

## 6. Conclusions

This paper proposed a new two-scale model for gradient-driven transport/flow in binary media: the extended distributed microstructure model (EDMM). The model is based on the distributed microstructure model (DMM) approaches of Szymkiewicz and Lewandowska [26] and Carr and

$K_b/K_a$	Model	ERROR	WALLTIME	STEPSIZE	KRYDIM
1	Fine-scale	n/a	00:33:41	0.3185	37
	Macroscopic	1.04e-03	00:00:01	0.6916	2
	Two-scale (DMM)	8.97e-03	00:07:47	0.5291	41
	Two-scale (EDMM)	1.08e-02	00:11:20	0.4026	40
$10^{-1}$	Fine-scale	n/a	00:48:23	0.2987	59
	Macroscopic	1.68e-03	00:00:01	0.6840	2
	Two-scale (DMM)	4.84e-03	00:02:55	0.6017	21
	Two-scale (EDMM)	5.54e-03	00:17:30	0.3873	57
$10^{-2}$	Fine-scale	n/a	00:54:13	0.2713	63
	Macroscopic	3.38e-03	00:00:01	0.6887	3
	Two-scale (DMM)	8.01e-03	00:00:50	0.6739	8
	Two-scale (EDMM)	6.30e-03	00:19:24	0.3597	60
$10^{-3}$	Fine-scale	n/a	00:59:11	0.2585	65
	Macroscopic	3.09e-02	00:00:02	0.6916	3
	Two-scale (DMM)	5.02e-03	00:00:31	0.7576	4
	Two-scale (EDMM)	3.96e-03	00:23:15	0.3571	63
$10^{-4}$	Fine-scale	n/a	01:25:36	0.2476	70
	Macroscopic	1.43e-01	00:00:03	0.6803	3
	Two-scale (DMM)	1.37e-03	00:00:32	0.7776	4
	Two-scale (EDMM)	1.20e-03	00:24:04	0.3785	70

Table 2: Simulation statistics for Case B: mean squared error along the line  $x_1 = 0.0125$  at  $t = 25$  hours using the fine-scale solution as the benchmark (ERROR), wall time in hours, minutes and seconds (hh:mm:ss) using 12 OpenMP threads (WALLTIME), mean time step size in seconds (STEPSIZE) and mean Krylov subspace dimension (KRYDIM). n/a – not applicable.

THREADS	WALLTIME	SPEEDUP
1	02:24:00	n/a
2	01:22:00	1.76
4	00:51:13	2.81
8	00:37:09	3.88
10	00:21:32	6.69

Table 3: Code speedup for EDMM applied to Case B: wall time in hours, minutes and seconds (hh:mm:ss) (WALLTIME) when increasing the number of OpenMP threads (THREADS) and resultant speedup factor relative to the single thread simulation (SPEEDUP). n/a – not applicable.

Turner [4] with several key advances. Most notably, the novel formulation defines the macroscopic flux as the average of the microscopic fluxes within the micro-cell. This is attractive because it avoids the use of traditional upscaling methods (such as homogenization or volume averaging) to derive the form of the macroscopic flux for a given microscopic constitutive law (bypassing the need for any effective parameters) and more accurately accounts for a non-equilibrium field in  $\mathcal{C}_{x,a}$  (part of the micro-cell occupied by the connected material  $a$ ). EDMM is also well-adapted to problems involving a micro-cell evolving over time (e.g., filter clogging, biofilm development, reactive or bio-active media).

The formulation was verified against the corresponding fine-scale model on a periodic domain, where the location and geometry of the micro-cells coincide precisely with the underlying heterogeneous geometry in the full domain. Numerical experiments demonstrated that both two-scale models (DMM and EDMM) produce numerical solutions that are in excellent agreement with the fine-scale model at a reduced computational cost. We found that DMM requires less computational cost (it is roughly 15 times faster than EDMM on average), however, EDMM is more accurate (reducing the error by a factor of 1.2 on average relative to DMM), able to capture additional features in the fine-scale solution and is closer to a completely general two-scale approach suitable for an arbitrary configuration.

This research forms part of an Australian Research Council (ARC) funded project on two-scale modeling and provides an intermediate step towards our long term goal of developing a two-scale model for multi-phase transport/flow capable of handling completely general heterogeneous media. Future research avenues will investigate problems involving micro-cells that do not completely tessellate the domain, extend the code to more sophisticated model equations (e.g., two-phase flow) and initiate an investigation into two-scale modeling for general non-binary heterogeneous media.

## Acknowledgements

This work was supported by Australian Research Council (ARC) grant DE150101137. The first author also thanks the Laboratory of Chemical Engineering & Materials (LGPM) and the Centre of Excellence for White Biotechnology (CEBB) at École Centrale Paris (now CentraleSupélec) for postdoctoral funding during 2013–2014. Additionally, the second author acknowledges the School of Mathematical Sciences at QUT for travel support during his visit to QUT in 2015. Finally, we gratefully acknowledge the authors of the open source software packages and libraries that made it possible to develop the code in this project and thank the two anonymous reviewers for their detailed analysis and suggestions that improved the quality of the final manuscript.

## Bibliography

- [1] A. Abdulle and W. E. Finite difference heterogeneous multi-scale method for homogenization problems. *J. Comput. Phys.*, 191:18–39, 2003.
- [2] T. Arbogast, Jr. J. Douglas, and U. Hornung. Derivation of the double porosity model of single phase flow via homogenization theory. *SIAM J. Math. Anal.*, 21(4):823–836, 1990.
- [3] J-L. Auriault. Heterogeneous medium: is an equivalent macroscopic description possible? *Int. J. Engng. Sci.*, 29(7):785–795, 1991.

- [4] E. J. Carr and I. W. Turner. Two-scale computational modelling of water flow in unsaturated soils containing irregular-shaped inclusions. *Int. J. Numer. Meth. Eng.*, 98(3):157–173, 2014.
- [5] E. J. Carr, T. J. Moroney, and I. W. Turner. Efficient simulation of unsaturated flow using exponential time integration. *Appl. Math. Comput.*, 217(14):6587–6596, 2011.
- [6] E. J. Carr, I. W. Turner, and P. Perré. A variable-stepsize Jacobian-free exponential integrator for simulating transport in heterogeneous porous media: application to wood drying. *J. Comput. Phys.*, 233:66–82, 2013.
- [7] E. J. Carr, I. W. Turner, and P. Perré. A dual-scale modelling approach for drying hygroscopic porous media. *Multiscale Model. Simul.*, 11(1):362–384, 2013.
- [8] F. Chen and L. Ren. Application of the finite difference heterogeneous multiscale method to the Richards’ equation. *Water Resour. Res.*, 44, 2007.
- [9] W. E. *Principles of multiscale modelling*. Cambridge University Press, New York, 2011.
- [10] W. E and B. Engquist. The heterogeneous multi-scale methods. *Commun. Math. Sci.*, pages 87–133, 2003.
- [11] W. E, B. Engquist, W. Ren, and E. Vanden-Eijnden. Heterogeneous multiscale methods: a review. *Comm. Comput. Phys.*, 3(3):367–450, 2007.
- [12] C. Guezaine and J-F. Remacle. Gmsh: A 3-d finite element mesh generator with built-in pre- and post-processing facilities. *Int. J. Numer. Meth. Eng.*, 79(11):1309–1331, 2009.
- [13] M. Hochbruck and A. Ostermann. Exponential integrators. *Acta Numerica*, pages 209–286, 2010.
- [14] I. G. Kevrekidis and G. Samaey. Equation-free multiscale computation: algorithms and applications. *Annu. Rev. Phys. Chem.*, 60(321–344), 2009.
- [15] I. G. Kevrekidis, C. W. Gear, J. M. Hyman, P. G. Kevrekidis, O. Runborg, and C. Theodoropoulos. Equation-free multiscale computation: enabling microscopic simulators to perform system-level tasks. *Commun. Math. Sci.*, 1(4):715–762, 2003.
- [16] J. Lewandowska and J. L. Laurent. Homogenization modeling and parametric study of moisture transfer in an unsaturated heterogeneous porous medium. *Transport in Porous Media*, 45:321–345, 2001.
- [17] J. Lewandowska, A. Szymkiewicz, K. Burzynski, and M. Vauclin. Modeling of unsaturated water flow in double-porosity soils by the homogenization approach. *Adv. Water Resour.*, 27: 283–296, 2004.
- [18] Y. Mualem. A new model for predicting the hydraulic conductivity of unsaturated porous media. *Water Resour. Res.*, 12(513–522), 1976.
- [19] P. Perré. Multiscale modelling of drying as a powerful extension of the macroscopic approach: application to solid wood and biomass processing. *Dry. Technol.*, 28(8):944–959, 2010.
- [20] A. J. Roberts, T. MacKenzie, and J. E. Bunder. A dynamical systems approach to simulating macroscale spatial dynamics in multiple dimensions. *J. Eng. Math.*, 86:175–207, 2014.
- [21] G. Samaey, D. Roose, and I. G. Kevrekidis. The gap-tooth scheme for homogenization problems. *Multiscale Model. Simul.*, 4(1):278–306, 2005.



- [22] G. Samaey, I. G. Kevrekidis, and D. Roose. Patch dynamics with buffers for homogenization problems. *J. Comput. Phys.*, 213:264–287, 2006.
- [23] R. E. Showalter. Microstructure models of porous media. In U. Hornung, editor, *Homogenization and Porous Media*, pages 183–202. Springer–Verlag, New York, 1997.
- [24] R. E. Showalter and N. J. Walkington. Diffusion of fluid in a fissured medium with microstructure. *SIAM J. Math. Anal.*, 22(6):1702–1722, 1991.
- [25] A. Szymkiewicz. Calculating effective conductivity of heterogeneous soils by homogenization. *Archives of Hydro-Engineering and Environmental Mechanics*, 52(2):111–130, 2005.
- [26] A. Szymkiewicz and J. Lewandowska. Unified macroscopic model for unsaturated water flow in soils of bimodal porosity. *Hydrolog. Sci. J.*, 51(6):1106–1124, 2006.
- [27] A. Szymkiewicz and J. Lewandowska. Micromechanical approach to unsaturated water flow in structured geomaterials by two-scale computations. *Acta Geotech.*, 3:37–47, 2008.
- [28] A. Szymkiewicz, J. Lewandowska, R. Angulo-Jaramillo, and J. Butlanska. Two-scale modeling of unsaturated water flow in a double-porosity medium under axisymmetric conditions. *Can. Geotech. J.*, 45:238–251, 2008.
- [29] Adam Szymkiewicz. *Modelling water flow in unsaturated porous media*. Springer, 2013.
- [30] M. T. van Genuchten. A closed-form equation for predicting the hydraulic conductivity of unsaturated soils. *Soil Sci. Soc. Am. J.*, 44(5):892–898, 1980.
- [31] S. Whitaker. Diffusion and dispersion in porous media. *AIChE Journal*, 13(3):420–427, 1967.
- [32] S. Whitaker. Coupled transport in multiphase systems: a theory of drying. In Y. I. Cho J. P. Hartnett, T. F. Irvine and G. A. Greene, editors, *Advances in Heat Transfer*, volume 31, pages 1–104. Elsevier, 1998.
- [33] X. Yue and W. E. Numerical methods for multiscale transport equations and application to two-phase porous media flow. *J. Comput. Phys.*, 210:656–675, 2005.
- [34] X. Yue and W. E. The local microscale problem in the multiscale modeling of strongly heterogeneous media: effects of boundary conditions and cell size. *J. Comput. Phys.*, 222:556–572, 2007.